REPORT DOCUMENTATION PAGE

Public reporting burden for this collection of information is estimated to average 1 hour per response, including the time for reviewing instructions, searching existing data sources, gathering and maintaining the data needed, and completing and reviewing the collection of information. Send comments regarding this burden estimate or any other aspect of this collection of information, including suggestions for reducing this burden, to Washington Headquarters Services, Directorate for Information Operations and Reports, 1215 Jefferson Davis Highway, Suite 1204, Arlington, VA 22202-4302, and to the Office of Management and Budget, Paperwork Reduction Project (0704-0188), Washington, DC 20503

1. AGENCY USE ONLY (Leave blank)	2. REPORT DATE July 1999	3. REPORT TYPE AND DATES COVERED Scientific Report

4. TITLE AND SUBTITLE Modeling and Control for Rapid Thermally Driven Deposition Processes	5. FUNDING NUMBERS N00014-98-C-0201

6. AUTHOR(S)
Abbas Emami-Naeini, Klavs F. Jensen, Sarbajit Ghosal, Vijay Gupta et al.

7. PERFORMING ORGANIZATION NAME(S) AND ADDRESS(ES) SC Solutions, Inc. 3211 Scott Blvd. Santa Clara, CA 95054	8. PERFORMING ORGANIZATION REPORT NUMBERS CVD-005

9. SPONSORING / MONITORING AGENCY NAME(S) AND ADDRESS(ES) Office of Naval Research Ballston Tower One 800 North Quincy Street Arlington, VA 22217-5660	10. SPONSORING / MONITORING AGENCY REPORT NUMBER

19990831 053

11. SUPPLEMENTARY NOTES

12a. DISTRIBUTION / AVAILABILITY STATEMENT Approved for Public Release; Distribution Unlimited	12b. DISTRIBUTION CODE

13. ABSTRACT (Maximum 200 words)

The objectives of this program were the study of the chemistry of YBCO thin film deposition by MOCVD, and the model-based control of MOCVD reactors. Model reduction techniques were applied to chemical vapor deposition (CVD) of YBCO thin films. This work has paralleled some of the work of Goodwin et al at Caltech sponsored under the DARPA VIP Phase I program, but with significantly different approach and emphasis. Under this program, the above chemistry was investigated from first principles using quantum chemistry computations (led by MIT). The kinetic and thermodynamic information obtained from these studies were used to generate a kinetic mechanism, which was then coupled to transport models for fluid flow, heat and mass transfer in CVD reactors. These coupled reaction-transport models were used to derive reduced order models for process control.

14. SUBJECT TERMS Chemical Vapor Deposition YBCO High Temperature Superconductors MOCVD	15. NUMBER OF PAGES 60
	16. PRICE CODE

17. SECURITY CLASSIFICATION UNCLASSIFIED	18. SECURITY CLASSIFICATION OF THIS PAGE UNCLASSIFIED	19. SECURITY CLASSIFICATION OF ABSTRACT UNCLASSIFIED	20. LIMITATION OF ABSTRACT
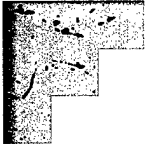
DTIC QUALITY INSPECTED 4

Modeling and Control for Rapid Thermally Driven Deposition Processes
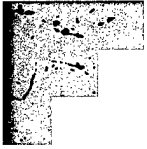
Final Technical Report

Period of Performance: June 21, 1998 to July 11, 1999
Contract No.: N00014-98-C-0201

Prepared for:

Dr. Stuart Wolf
Defense Advanced Research Projects Agency (DARPA)
DSO
3701 North Fairfax Drive
Arlington, VA 22203-1714

Dr. Steve Fishman, ONR 332
Office of Naval Research
Ballston Tower One
800 North Quincy Street
Arlington, VA 22217-5660

SC Solutions, Inc.
3211 Scott Blvd., Santa Clara, CA 95054
(tel) 408-486-6060, (fax) 408-486-6083
Email: emami@scsolutions.com

SC Report No.: CVD-005

July 2, 1999

Modeling and Control for Rapid Thermally Driven Deposition Processes

Final Technical Report

Period of Performance: June 21, 1998 to July 11, 1999
Contract No.: N00014-98-C-0201

Prepared by:

Abbas Emami-Naeini	Klavs F. Jensen	Ioannis G. Kevrekidis
Sarbajit Ghosal	Vijay Gupta	S. Shvartsman
Jon L. Ebert		C. Theodoropoulos
Dick de Roover		
Robert L. Kosut		
SC Solutions, Inc.	**Massachusetts Institute of Technology**	**Princeton University**

Prepared for:

Dr. Stuart Wolf
Defense Advanced Research Projects Agency (DARPA)
DSO
3701 North Fairfax Drive
Arlington, VA 22203-1714

Dr. Steve Fishman, ONR 332
Office of Naval Research
Ballston Tower One
800 North Quincy Street
Arlington, VA 22217-5660

SC Solutions, Inc.
3211 Scott Blvd., Santa Clara, CA 95054
(tel) 408-486-6060, (fax) 408-486-6083
Email: emami@scsolutions.com

SC Report No.: CVD-005

July 2, 1999

Table of Contents

List of Figures

ABSTRACT

The objectives of this program were the study of the chemistry of YBCO thin film deposition by MOCVD, and the model-based control of MOCVD reactors. Model reduction techniques were applied to chemical vapor deposition (CVD) of YBCO thin films. This work has paralleled some of the work of Goodwin *et al* at Caltech sponsored under the DARPA VIP Phase I program, but with significantly different approach and emphasis.

Under this program, the above chemistry was investigated from first principles using quantum chemistry computations (led by MIT). The kinetic and thermodynamic information obtained from these studies were used to generate a kinetic mechanism, which was then coupled to transport models for fluid flow, heat and mass transfer in CVD reactors. These coupled reaction-transport models were used to derive reduced order models for process control. In addition, effort was directed toward model reduction (led by SC Solutions and Princeton University).

SC Solutions implemented the CVD modeling techniques on a commercially available CFD/CVD software. Because of its wide acceptance in the semiconductor industry, we selected CFD-ACE from CFDRC as the prototype platform. In particular, SC Solutions developed a model of a system used by Superconductor Technologies Inc. (STI) for deposition of YBCO high thin films using CFD-ACE.

Executive Summary

SC Solutions, MIT, and Princeton have developed computer simulation tools and control strategies for production of yttrium-barium-copper oxide ($YBa_2Cu_3O_{7-x}$ or YBCO) thin films with high temperature superconducting (HTS) properties, using metal-organic chemical vapor deposition (MOCVD) process. HTS thin films have applications in high speed-low power computing and signal processing electronics, high performance microwave devices, magnetic sensors, and in optoelectronic systems for communications and signal analysis. MOCVD offers the potential for growth under highly oxidizing conditions, for large area deposition, and high throughput. Our research on CVD modeling involves concurrent development of first principles chemical mechanisms with reactor scale modeling to provide a more realistic description of MOCVD reactors. Earlier, very little was known of the chemical mechanism involved in decomposition of metal precursors and oxide formation both in gas-phase and at the wafer surface. There had not been any systematic investigation of control issues for better control of growth rates, oxide stoichiometry, and film thickness uniformity. Our team has successfully addressed the above issues through fundamental quantum-mechanical calculations, reactor-scale physical process model, model order reduction, and developing model-based control strategies. These simulation tools and the results obtained from the studies provides a clear understanding of the chemical mechanism, species transport, and film growth. This understanding enables design and implementation of optimized controllers and that meet both process specifications as well as run-to-run repeatability which is essential for large-scale production. The following summarizes the research results in more detail.

First, principle quantum chemistry calculations have been performed to probe the reaction pathways in the decomposition of metal β-diketonates, used as precursors for this CVD process. The metal β-diketonates can be represented by the general formula $M(R_1C(O)CHC(O)R_2)_n$ where M is the metal (M = Cu, Y), R_1 and R_2 are the substituents on the ligand ($R_1=R_2=CH_3$ for acac and t-butyl for dpm) and n denotes the number of ligands (n=2 for Cu, n=3 for Y). There is very little information available on these compounds which makes the choice of the method difficult. Different methods and basis sets have been tested and evaluated by comparing model predictions against experimental data for small copper compounds having similar bonds as the copper β-diketonates. Based on our validation studies, hybrid density functional theory method, particularly the implementation using the three parameter Becke exchange and the Lee-Yang-Parr correlation functionals (B3LYP), was chosen. For copper, we used the effective core potentials by Hay and Wadt [1-3] with a Neon core with the associated double zeta basis set. The Dunning/Huzinga full double zeta (D95) basis set was used for all other elements.

Mean bond dissociation energies (BDE) of the M-O bond (M = Cu, Y) and the scission of the substituents R_1, R_2 (CH_3 and t-butyl) from the ligand have been determined. Relative magnitudes of the bond strengths suggest the break-up of the chelate ring as the initial step, followed by the cleavage of the t-butyl (or CH_3) group from the precursor. This is accompanied by further break-up of the entire organic structure. The Cu-O bond rupture seems to be the rate-controlling step. Based on these observations, a kinetic mechanism has been formulated. Rate parameters have been estimated for the rate-controlling step and they correlate well with the rate parameters obtained from the overall decomposition process using mass-spectrometry.

Structures obtained for $Y(acac)_3$ are in good agreement with experimental data. The Y-O bond strength is higher compared to the Cu-O bond strength in $Cu(acac)_2$. Morokuma's "our own n-layered integrated molecular orbital and molecular mechanics" (ONIOM) method [4] allows the treatment of different parts of a molecule at different levels of theory, and has been used to study

6

the precursor, Y(dpm)$_3$. The bulky t-butyl t-butyl groups have been treated using molecular mechanics and the central rings are treated using DFT methods. Y(acac)$_3$ has been used as a model compound for Y(dpm)$_3$ in some cases. The decomposition is initiated by the cleavage of the t-butyl group followed by ligand pruning to give Y(dpm)$_2$. These results are in agreement with experimental observations.

HTS MOCVD models were developed for the 2D version of the commercial STI reactor using CFD-ACE, and deposition rates and film thickness uniformity of YBCO films were obtained. The deposition rates compare favorably with the published literature and the experimental results from STI. Results were obtained on Principal Orthogonal Decomposition (POD)-based compression of two kinetic schemes. A general control structure was developed for MOCVD reactor control systems. An innovative run-to-run controller scheme was developed that enables efficient convergence to the desired stoichiometry region for MOCVD systems using a multi-step process control method.

Accomplishments

- Developed a systematic methodology and formulated strategy to understand the chemical mechanism involved in MOCVD of YBCO thin-films.
- Undertook fundamental investigation using density functional theory for quantum-mechanical calculations to determine most probable pathways for precursor decomposition and oxide formation leading to YBCO thin-film growth. These calculations have greatly increased understanding of precursor decomposition. They studies resolved controversies in the literature, namely the existence of some gas-phase reactions as part of the decomposition mechanism.
- This quantum chemistry methodology allows determination of rate constants, etc., in absence of difficult and costly experiments, and allows determination of the effects of impurities
- The above approach for elucidating the chemical mechanism involved in the decomposition of such large molecules is a pioneering effort!
- A two-dimensional MOCVD reactor-scale model, developed using an approximate chemical mechanism, has been used for calculating growth rate, deposition uniformity, and oxide stoichiometry at wafer surface. Results comparable to those in the literature and those recorded at an industrial reactor (STI, Santa Barbara, CA). The model was refined using rate constants from the DFT calculations.
- Control architecture has been developed for both run-to-run and real-time feedback. Response surface maps were used to develop model-based controllers for better uniformity, and for run-to-run variations due to bubbler temperature drift, etc. The developed run-to-run control scheme allows control of stoichiometries of Ba, Y, and Cu of the YBCO thin film. The scheme is very innovative as the process model can be used in lieu of costly experiments to provide quick convergence to the desired stoichimetry region.

Acknowledgements

1. Introduction and Background on HTS and CVD Modeling

HTS

High temperature superconductivity (HTS) has applications in technologies such as high-speed, low-power computing and signal processing circuits, high performance microwave devices, magnetic sensors, and optoelectronic systems for communications and signal analysis. These materials have several potential applications, including magnetic film detection, fast computing devices, interconnects for multichip modules, bolometric detectors, and microwave devices. Complex oxide materials are used in thin film form to make such devices and circuits.

CVD Modeling

The focus of this research effort was on chemical mechanism generation and reduction for metalorganic chemical vapor deposition (MOCVD) of high temperature superconducting (HTS) films. As a technique for fabrication of HTS films, MOCVD offers the potential for growth under highly oxidizing conditions, for large area deposition, and high throughput. However, the process is highly complex involving flow, heat transfer, and gas-phase and surface chemical kinetics at high temperatures. The decomposition reactions of the precursors are crucial to the process. Typical precursors for the growth of $YBa_2Cu_3O_{7-x}$ films are β-diketonates, e.g., $Ba(dpm)_2$ (dpm=3D dipivaloylmethanate) or $Ba(hfa)_2=B_7tet$ (hfa=3D hexafluoroacetylacetonate, tet=3D tetraglyme). These precursors are typically difficult to transport and their decomposition mechanisms are poorly characterized. The current understanding of MOCVD of HTS films is limited to conditions leading to mass transport or kinetically limited growth regimes. Semi-empirical models based on assumptions of a few gas-phase reaction steps followed by overall surface reactions have been proposed, but the chemical mechanisms underlying MOCVD is not understood. An improved understanding of the basic chemistry could lead to process improvements and would provide the basis for model-based process control algorithms through the use of nonlinear model reduction techniques. These issues were addressed in this program.

2. Gas-Phase Chemistry of High Temperature Superconductors

Introduction

Many fundamental challenges in the growth of high temperature superconductor (HTS) films by metalorganic chemical vapor deposition (MOCVD) are associated with the properties of the precursor compounds [5-8]. Metal β–diketonates are the most widely used precursors and have the general formula $M(R_1C(O)CHC(O)R_2)_n$, where M is the metal atom, R_1 and R_2 are the substituents in the ligand and n is the number of ligands in the complex. Some of the common substituents employed in HTS film deposition are $R_1 = R_2 = CH_3$ (acetylacetonate, acac), $R_1 = R_2 = C(CH_3)_3$ (dipivaloymethanate, dpm) and $R_1 = R_2 = C(CF)_3$ (hexafluroracetylacetonate, hfac). The general structure of a copper β-diketonate is shown in Figure 1. MOCVD of HTS films is a complex process involving both gas-phase and surface reactions. Deposition of HTS films of definite composition requires the knowledge of decomposition products and kinetic parameters. Choice of the substituents on the ligand influences the volatility and thermal stability of the precursor molecule. The precursor molecules are typically solids at room temperature. They are either vaporized before transporting to the deposition chamber, or are dissolved in an organic solvent and then delivered via aerosol delivery to the deposition chamber. The latter process is complicated by combustion of the organic solvent molecules. The reactant gases are mixed with an oxidant gas such as O_2, N_2O [9] or O_3 [10] and undergo decomposition and oxidation over the heated substrate to deposit a film of the desired material.
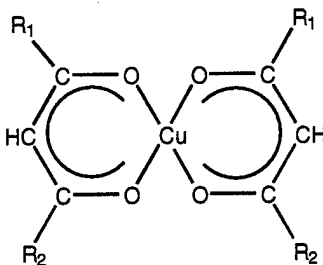
Figure 1. Schematic of the Cu β-diketonate.

$YBa_2Cu_3O_7$ is the most widely studied HTS material. Common precursors in the MOCVD of YBCuO films are $Y(dpm)_3$, $Ba(dpm)_2$ $Cu(acac)_2$ and $Cu(dpm)_2$. There are very limited experimental data for the thermolysis and oxidation of the metal β-diketonate compounds. Only recently, kinetic studies using mass spectroscopy and FTIR spectroscopy have begun to appear.

The gas-phase reactions in the CVD chamber can have a marked influence on film properties such as uniformity, impurity incorporation and deposition rates. For example, films grown using the hfac ligand are found to have a high fluorine contamination. Similarly, using N_2O as the oxidant gas (in place of O_2) lowers the substrate temperature requirements, but also decreases the growth rate by a factor of two [11].

We have used quantum chemistry methods to explore the different reaction pathways to gain an understanding of the structure and reactivity of the precursor molecules. The attention particularly focused on determination of the initial step in the decomposition process. Information on the subsequent reaction steps involving the organic products can then be obtained from the extensive literature available in the field of combustion chemistry [12]. The kinetic and thermodynamic information obtained from these studies can be used to generate a kinetic mechanism, which can then be coupled to transport models for fluid flow, heat and mass transfer in CVD reactors. These coupled reaction-transport models can be used to derive reduced order models for process control.

Computational Details:

Gaussian98 suite of programs [13] was used for all calculations, except the validation calculations where Gaussian94 and MOLPRO [14] were also used. The hybrid DFT approach was used with the three parameter Becke exchange [15], and the Lee-Yang-Parr correlation functionals [16] (B3LYP). For copper, we used the effective core potentials by Hay and Wadt [1-3] with a Neon core with the associated double zeta basis set, and the Dunning/Huzinga full double zeta (D95) basis set for all other elements. This combination is referred to as ECP II here. The choice of this method/basis set combination is the result of a detailed testing of different methods and basis sets and comparing the results with experimental data. This is described in the subsequent paragraphs.

Validation of Methods and Basis Sets

The application of quantum chemistry (QC) methods to the precursors employed in CVD of high temperature superconductors is a challenging task due to the large number of electrons (many of them core), electron correlation and increased importance of relativistic effects for large nuclei. To control the computational time needed for the calculations, two parameters can be varied: calculation method and eventually the basis set.

Traditionally, three types of methods have been distinguished: empirical, semi-empirical and ab-initio calculations. For molecules of the size used in the current project, semi-empirical and ab-initio methods are the most common ones. In case of the ab-initio methods, two subgroups can be divided, i.e. density functional theory (DFT) and 'traditional' ab-initio methods like Hartree-Fock (HF), Moller-Plesset perturbation theory (MPx) or configuration interaction (CI). Depending on the level of accuracy, the 'traditional' methods include different amounts of the correlation energy in the system, however, they also require more computational time with increasing accuracy. This is due to the unfavorable scaling with the number of electrons in the system for the modest- to high-level methods (like CI). DFT methods, on the other hand, generally include the correlation energy, but scale much more favorable. However, the crux lies in the suitable choice of the density functionals applied, which is still not fully understood due to the relatively new nature of the DFT method itself.

During the last two years, hybrid methods like Morokuma's ONIOM [17, 18] have been developed, which can couple any of the three types of methods in a single calculation on a single system. In this case, high accuracy methods might be used for atoms at the reaction center and computational less expensive ones for atoms in the periphery.

The common type of a basis set treats every single electron in the system, which is to be described. Using these all-electron basis sets, going down one row in the periodic, the computational cost can increase by up to a factor of ten. A better approach is the use of the effective core potentials (ECPs), where the electronically less important core electrons are

replaced with a small number of potentials, resulting in substantial savings in time, memory and disk space requirements. As a further advantage, they often include Darwin and mass-velocity relativistic effects. However, the decision which electrons are put into the core and which are explicitly described by basis functions is often crucial to the performance of the ECPs. For instance, in the case of transition metals (electronic configuration [...] $(n-1)s^2$ $(n-1)p^6$ $(n-1)d^x$ ns^y np^0) the correlation between (n-1) s,p electrons and the $(n-1)d$ electrons can be so strong that the whole (n-1) shell has to be excluded from the core.

Finding a combination of method and basis sets, which does not exceed a reasonable amount of computer resources, but still give sufficiently accurate results, is one of the first tasks in any computational project. In the current project, the challenge was that experimental and computational data for the investigated systems are sparse and are not sufficient to check the accuracy of our calculations. Therefore, an evaluation of different methods/basis set combination was done on smaller systems, which include the bond types involved in the current systems.

Semiempirical – PM3

The large size of the precursor molecules would suggest the use of semi-empirical models, if applicable. PM3™ [19], a semi-empirical method, parameterized for transition metals has been implemented in Spartan [20] and its use was initially explored for bis-acetylacetonate copper (II). Its structure has been determined to have copper in square-planar coordination and the two ligands lying in one plane [21, 22]. However, a geometry optimization using the PM3™ method does not agree at all with the experimental results, but rather suggests a contorted structure where the carbon atoms of one ligand are tipped up relative to the rest of the molecule by almost exactly 90°. Therefore, this approach was considered inadequate for the systems investigated.

Ab initio – DFT

As the systems to be investigated in this project are relatively large, we did not consider 'traditional' ab initio methods of a sufficient accuracy (MPx, CI) to be reasonable in terms of computational time. Instead, we were focusing on the DFT methods, checking different functionals. These functionals (and combinations, respectively) were:
(1) Becke's correlation functional [15] together with the correlation functional of Lee, Yang and Parr [16] (BLYP)
(2) Becke's 3-parameter hybrid functional [23] together with the correlation functional of Lee, Yang and Parr [16] (B3LYP)
(3) Slater exchange functional [24-26] together with Vosko, Wilk and Nusair's correlation functional [27] (LSDA)
Configuration interaction (CI) and Coupled Cluster methods (e.g. CCSD(T)) were used only for comparison, as they are considered to treat correlation with a high accuracy.

For the basis functions, two all-electron basis set (6-311G with/without diffuse (+)/polarization (*) functions and Ahlrich's triple-ζ valence [tzv]) were compared with combinations of Hay and Wadt's effective core potentials (Cu) and appropriate basis sets for all other atoms (ECP1/STO3-G [ECP1] and ECP2/D95 [ECP2]). In some cases, the Stuttgart ECP has also been used [28]. There had been doubts about the applicability of Hay and Wadt's ECPs, along with their associated valence basis sets, for DFT calculations. In a study on $CuCH_2$ [29], the Hay-Wadt's ECPs have been checked for DFT work and the concerns dismissed.

The systems used for the evaluation of the different bonds were:

general electronic structure	Cu: ionization potential [IP], excitation energy [E_{exec}]
Cu-H	Cu-H
Cu-C	Methyl-copper (CuMe), Ethyl-copper (CuEt)
Cu-O	Hydroxy-copper (CuOH), Copper-dimethylate (Cu(OMe)$_2$), Copper monoxide (CuO)

CC, CO and CH bonds have not been evaluated, because they have been tested extensively throughout the literature and found to be described with good accuracy by the methods/basis sets in question. Data for the validation studies are given in Appendix I.

Cu

The calculations showed that the excitation energy ^2S -> ^2D can only be computed reasonably, if the correlation energy is included to a high extent (as in CCSD(T)). DFT calculations (like B3LYP) do not even give qualitatively correct results. Not much difference has been seen for the different ECPs.

The ionization potential is much less sensitive to correlation and therefore DFT methods are giving reasonably accurate results. B3LYP was found to perform extremely well, with errors not more than 6(2) kcal/mol for all-electron (ECPs), except if 6-311G is used without polarization/diffuse functions.

CuH

For CuH a short evaluation of data showed the influence of the correlation on the dissociation energy, if B3LYP is used. In this case, ECP1 did not perform well, due to the relatively large core. ECP2 and 6-311+G**, on the other hand, showed about the same quality as highly correlated CI calculations (including core-core correlation).

CuMe, CuEt

For methyl-copper some experimental data (vibrational frequencies, estimate of dissociation energy) are available, which makes it a good testing candidate. The drawback, however, is the pronounced anharmonicity of the methyl group, which will show as a disagreement between the experimental set of vibrational frequencies (including anharmonicity) and the calculated harmonic fundamentals (without anharmonicity, as the name implies).

The calculated dissociation energies (exp. 60 kcal/mol) for CuMe (6-311+G**, ECP1, ECP2) are too high for LSDA calculations, which is usual for this method. BLYP calculations are within 10 kcal/mol of the experimental estimate, with the exception of ECP2, which performs surprisingly poorly (35 kcal/mol difference). B3LYP calculations showed good agreement, with 6-311+G** and ECP2 about the same value (52.4 kcal/mol and 53.7 kcal/mol). ECP1 gives a slightly higher value (59.1 kcal). With CuEt it has been shown that the diffuse function (+) in the 6-311G basis set is crucial to the accuracy. Polarization functions (**) on the other hand, only slightly change the calculated energy difference (0.7 kcal/mol).

To further evaluate the quality of the basis sets, the basis superposition error was calculated for 6-311+G** (-5.6 kcal/mol), ECP1 (8.0 kcal/mol) and ECP2 (-2.9 kcal/mol). The

14

relative high value for the ECP1 shows that this ECP/basis set combination is not flexible enough to correctly describe the electron distribution in the system. The values for 6-311+G** and ECP2 are considered to be reasonable, especially because relaxation of the methyl radical after dissociation has not been taken into the correction. Correction of the dissociation energy using the BSSE gives 6-311+G** and ECP2 values within 3.5 kcal/mol of the experimental estimate and extremely close to the values of Ziegler [30] and Boehme [31]. The calculated frequencies were compared with the experimental data set for 6-311+G**, ECP1 and ECP2. The CH vibrations are usually about 2-10% overestimated by our calculations (6-311+G** and ECP2), but come out 12-20% too high, if ECP1 is used. For the Cu-Me vibrations (stretch and tilt) 50-60% overestimation seem to be common, with the Cu-Me tilt being more off. Particularly bad performing are B3LYP/ECP1 and all basis sets under LSDA (up to 75% overestimation). These relatively high errors are probably due to anharmonicity as well as method/basis set insufficiency. However, no information can be obtained on how much each of these factors account for.

For CuEt similar calculations have been performed, but could not be compared to any experimental data. A factor $f = \omega(B3LYP/X)/\omega(B3LYP/6-311G)$ has been introduced to compare the calculational data. However, this factor is close to 1 for all basis sets under B3LYP and almost all frequencies (except for the Cu – C=C stretch). No particular difference regarding the ECP1 could be seen.

Cu-O bond
To check the applicability of the methods regarding the most important bond in the present systems, different models could be thought of. The one being chemically similar are copper alkoxides like $Cu(OMe)_2$. Unfortunately these compounds are unstable towards hydrolysis and therefore experimental data are sparse. Additionally, the experimental data available are obtained from solid state where copper has square-planar coordination.

These differences are believed to lead to the considerable problems faced when trying to calculate this system as a gas phase molecule. For B3LYP/6-311G** and B3LYP/ECP2 geometry optimizations converged and harmonic frequencies were compared with the experimental ones. Again, an overestimation of 20 – 35 % is seen, however, data did not allow for a further analysis.

Instead, CuOH and CuO were used to check for the calculation of the Cu-O bond, although these bonds have no chemical similarity to the Cu-O bond in the investigated systems. CuOH geometries, dissociation energies and frequencies were compared with ECP1 and ECP2 using B3LYP and SD-CI methods. It again becomes clear that B3LYP/ECP2 is close in accuracy to all-electron calculations and SD-CI calculations, but ECP1 is not applicable.

The calculated dissociation energies for CuO show again an overestimation by at least 20-30 kcal/mol for LSDA calculations and good agreement for B3LYP/6-311+G** and B3LYP/ECP2. However, in contrast to the calculations at CuMe/CuEt, the diffuse function does not improve the accuracy if no polarization function are present.

Summary of gas-phase chemistry

The above validation of basis sets and methods show that out of the 3 tested functional combinations for DFT calculations, B3LYP gives generally the best results compared with the experimental data. Regarding the basis set, either an all-electron triple-zeta basis set (6-311G) or a Ne core ECP (ECP2) can be used with good results. However, for the all-electron basis set, it is

important to include both diffuse and polarization functions as they influence different kinds of bonds in different ways.

Structures

Structural parameters obtained from quantum chemistry calculations were compared against experimental data for Cu(acac)$_2$ [21, 22] and Y(dpm)$_3$ [32], obtained from electron diffraction studies, and were found to be in good agreement. Both Cu(acac)$_2$ and Cu(dpm)$_2$ have copper in a square-planar coordination with Cu-O bond length of ~ 1.95 Å. Y(acac)$_3$ has a traiganol prismatic structure with Y-O bond ~ 2.260 Å which shortens to 2.155 A in Y(acac)$_2$. This is in qualitative agreement with the structure for Y(dpm)$_3$ obtained from gas phase electron diffraction data [32, 33]. The effect of replacing the substituent alkyl group on the ligand (CH$_3$ in acac and C(CH$_3$)$_3$ in dpm) with H atoms (giving the 3-oxo-propen-1-olate ligand, opo ligand) on the ring structure was investigated and found to be negligible. Hence for geometry optimizations, the terminal group on the ligand was replaced with H atoms to determine the skeletal ring structure, which was then used as a starting guess for further optimizations.

The acetylacetonate radical (acac) can exist in different conformations (3 in the keto form and 1 in the enol form) [34]. The different conformations are shown in figure 2 and the relative energies for the structures are given in table 1.

1.

2.

3.

4.
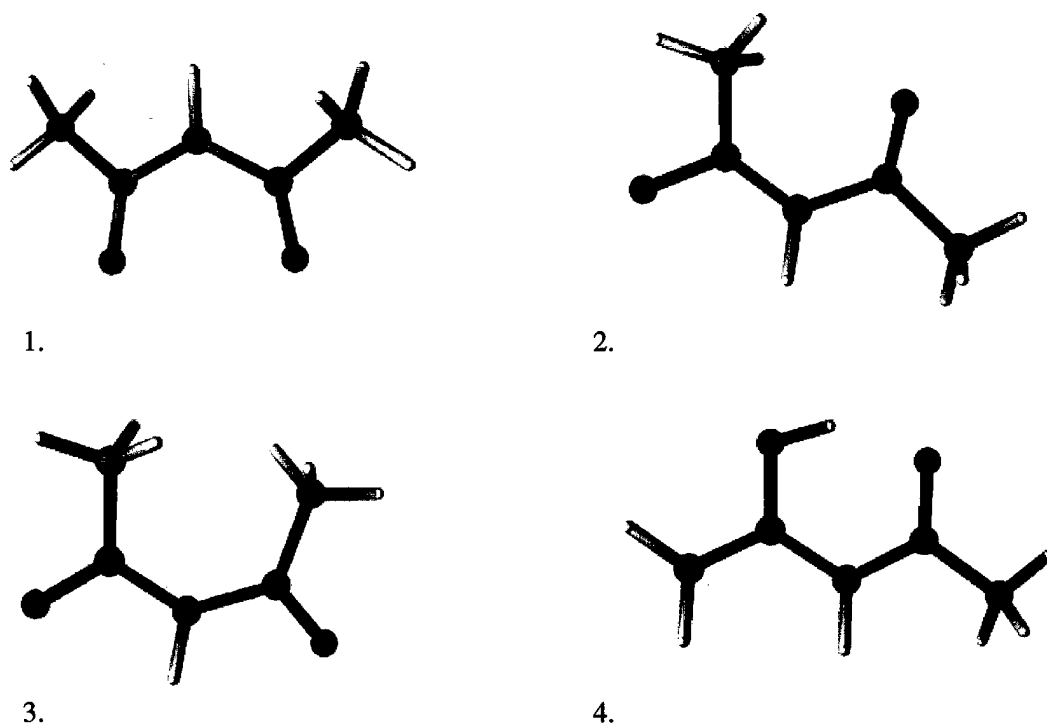
Figure 2. Different possible conformations for the acac ligand.

16

Conformation	E° (hartrees)	ZPE (hartrees)	E° + ZPE (hartrees)	Relative Energy (kcal/mol)
acac **1.**	-345.0892	0.1082	-344.9810	0.0
acac **2.**	-345.0737	0.1092	-344.9644	10.4
acac **3.**	-345.0933	0.1091	-344.9842	-2.2
acac enol **4.**	-345.1065	0.1099	-344.9966	-9.8

Table 1. Relative energies for the different conformations for the acac ligand radical.

Precursor Decomposition Pathways

1. Copper Precursors:

Decomposition of $Cu(acac)_2$ and $Cu(dpm)_2$ can be initiated via two different pathways:

(a) Dissociation of the substituent (CH_3 for acac and t-butyl for dpm) on the ligand ring to give the corresponding radical, leaving the central ring intact.

(b) Dissociation of the ligand from the central copper atom causing the breakup of the ring structure leaving the bare metal atom behind. This may occur in a single step or in multiple steps.

The energy required to break the necessary bonds gives the relative strength of the bonds and the bond dissociation energies (BDE) can be used to determine the initial step in the thermal decomposition of these precursor molecules.
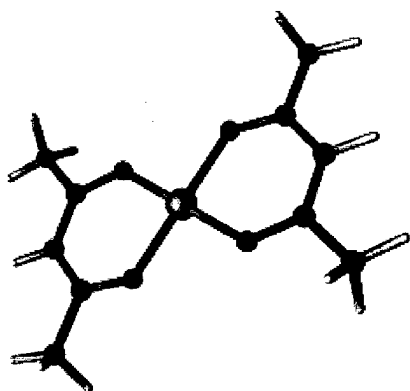
Figure 3. Optimized structure for $(acac)_2$.
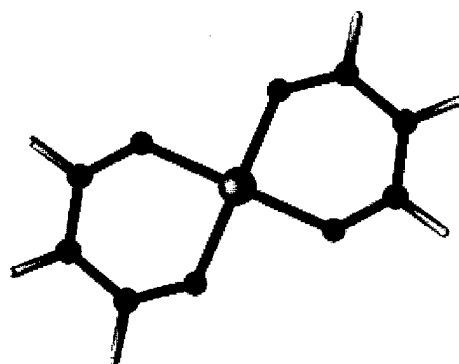
Figure 4. Optimized structure for Cu β–diketonate, with terminal R replaced by H.

17

The nature of the Cu-O bond does not change with the change in the terminal alkyl group on the ligand and the bond strength of the Cu-O bond should be similar for the different Cu β-diketonates. In order to reduce the computational cost involved in this study, the effect of replacing the terminal *t*-butyl groups by H as well as CH_3 was studied. As reported earlier, this has no influence on the geometry of the ring structure around the central copper atom. The mean Cu-O strength was determined as follows

$$BDE (Cu-O) = [E(Cu.L_2) - E(Cu) - 2 E (L)] / 4$$

where   E is the zero-point corrected ground state energy.
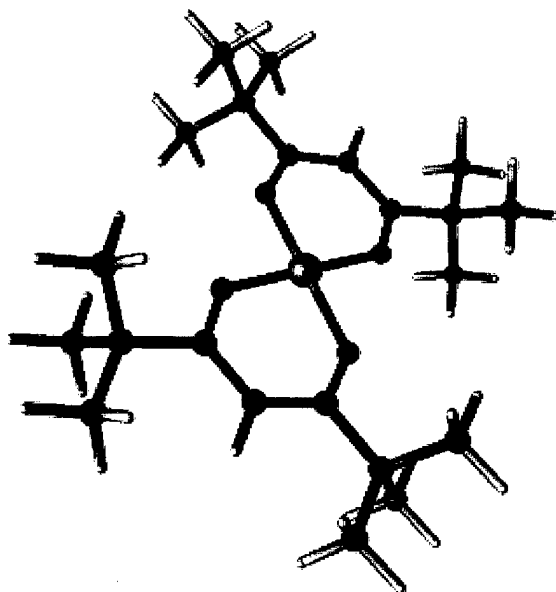
Figure 5. Optimized structure for Cu(dpm)$_2$

Species	R	BDE (Cu-O) (No ZPE corr.)	BDE(Cu-O) (ZPE corrected)	BDE(Cu-O) Experimental [35]
Cu(opo)$_2$	H	5.2	3.8	-
Cu(acac)$_2$	CH3	40.1	38.5	39.9 ± 2.4
Cu(dpm)$_2$	C(CH$_3$)$_3$	39.1	37.9	40.2 ± 2.4
Cu(hfac)$_2$	CF$_3$	42.8	41.8	39.2 ± 2.6

Table 2. Mean Bond Dissociation Energies (BDE) for different substituent groups on the Cu β–diketonate precursor. Energy is in kcal/mol.

The mean bond dissociation energy for Cu-O bond in Cu(acac)$_2$ and Cu(dpm)$_2$ is ~ 40 kcal/mol. The calculated BDE energy for Cu(opo)$_2$ gives a value of ~ 4 kcal/mol. Since the terminal alkyl groups do not influence the Cu-O bond strengths considerably, these results indicate that the substitution of the t-butyl group by an H atom is invalid. The reason is apparent when one considers the products of the Cu-O bonds dissociation. The β–diketonate breaks up to give Cu and two ligand radicals. The radical (CH$_3$)$_3$C-C(O)CHC(O)-C(CH$_3$)$_3$, formed from the

breakup of the $Cu(dpm)_2$, is a stable species, whereas, the radical $HC(O)CHC(O)H$, is highly unstable. Calculations done with $R=CH_3$ give excellent agreement with the energies obtained with $R=C(CH_3)_3$. Hence for all further calculations, the t-butyl can be replaced by CH_3, resulting in considerable savings in computational time and effort.

The C-C bond strength for the loss of the t-butyl group from $Cu(dpm)_2$ is 72 kcal/mol. The corresponding bond strength for the removal of the CH_3 radical is 90 kcal/mol. These values are considerably higher than the mean Cu-O bond strength and hence Cu-O bond will break first followed by the loss of the t-butyl or the methyl group. This is consistent with experimental observations for thermal decomposition of $Cu(dpm)_2$ where the IR absorption due to the ring structure begins to decrease earlier than the IR absorption for the $C-H_x$ stretch of the t-butyl group [36, 37].

The decomposition is thus initiated by the break-up of one Cu-O bond to form a complex with one bidentate ligand and one monodentate ligand. The monodentate ligand rearranges itself to a more stable conformation and the resulting complex is depicted in
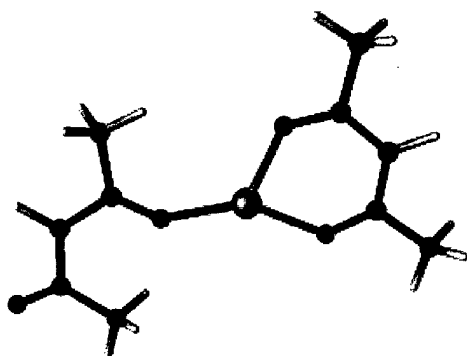
Figure 6. Structure for the $Cu(acac)_2$ with one monodentate ligand after the break-up of the Cu-O bond.
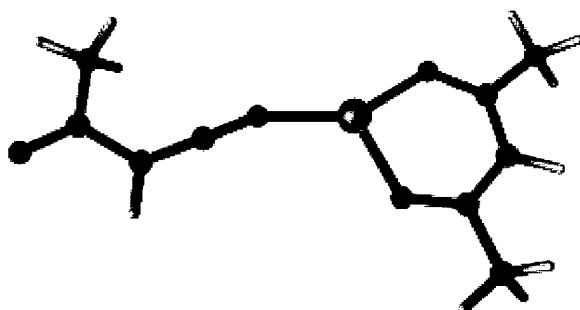
Fig. 7 (a)   Fig. 7 (b)
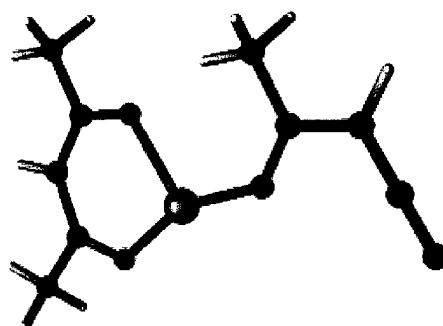
Figure 7. Optimized structures for the loss of CH_3 radical from the monodentate ligand of $Cu(acac)_2$. (a) CH_3 close to the Cu atom is lost (b) CH_3 away from the Cu atom is lost.

19

The second step is the splitting of the CH$_3$ radical from the monodentate ligand. This can take place in two different ways: (a) CH$_3$ close to the central Cu atom breaks off or (b) the CH$_3$ further from the Cu atom breaks up. Depending on which CH$_3$ splits off, we may get different products.

For case (a), the Cu-O bond between the monodentate ligand and the Cu atom breaks and we get CH$_3$(CO)CH(CO) radical and Cu(acac) which can further break up to give acac ligand and Cu. For case (b), the intact bidentate acac ligand can abstract an H from the monodentate ligand forming Hacac, and the monodentate ligand breaks up forming ketene (CH$_2$=C=O) and CH$_3$CO radical. The initial Cu-O bond splitting is the rate-determining step. The final products are the Cu atom and hydrocarbons. The chemistry of the hydrocarbons is fairly well known from combustion chemistry [12, 38]. The bare Cu atom gets oxidized to give CuO and Cu$_2$O.

In the case of Cu(dpm)$_2$, we get t-butyl radicals (instead of CH$_3$) which can further disproportionate to give butene and butane, which have been observed experimentally during thermal decomposition of Cu(dpm)$_2$ using FTIR spectroscopy [39, 40].

The above observations can be used to formulate a kinetic mechanism.

Copper Acetylacetonate:

Cu(acac)$_2$	→ Cu(acac*)(acac)
Cu(acac*)(acac)	→ Cu(acac) (CH$_3$COCHCO) + CH$_3$
Cu(acac) (COCHCOCH$_3$)	→ Cu + CH$_2$CO + Hacac + CHCO
	→ Cu(acac) + CH$_3$COCHCO
** Cu(acac)	→ Cu + acac
Cu + O$_2$	→ CuO$_2$
Cu + CuO$_2$	→ 2 CuO
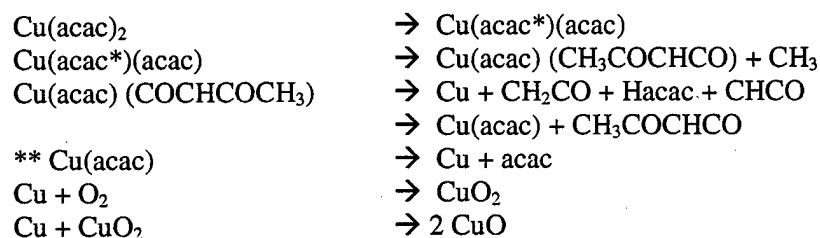
acac* denotes the ligands as being monodentate.

CH$_2$CO, CHCO, Hacac, CH$_3$COCHCO are hydrocarbons whose decomposition and oxidation chemistry is well known from combustion literature.

Copper Dipivaolylmethanate:

Cu(dpm)$_2$	→ Cu(dpm) + (COCHCOC$_4$H$_9$) + C$_4$H$_9$
Cu(dpm)$_2$	→ Cu(dpm)(COCHCOC$_4$H$_9$) + C$_4$H$_9$
Cu(dpm)(COCHCOC$_4$H$_9$)	→ Cu + Hdpm + C$_4$H$_8$ + CHCO + CO
C$_4$H$_9$COCHCO	→ C$_4$H$_8$ + CH$_2$CO + CO
2 C$_4$H$_9$	→ C$_4$H$_8$ + C$_4$H$_{10}$
** Cu(dpm)	→ Cu + dpm
2 C$_4$H$_9$	→ C$_4$H$_8$ + C$_4$H$_{10}$
Cu + O$_2$	→ CuO$_2$
Cu + CuO$_2$	→ 2 CuO
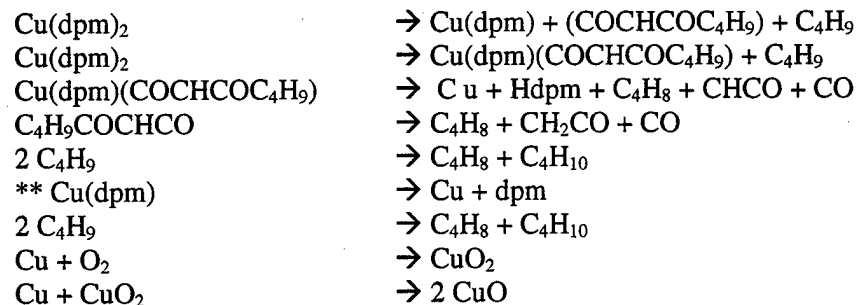
** Cu(acac) and Cu(dpm) could also dissociate via

Cu(acac)	→ CuO + hydrocarbons
Cu(dpm)	→ CuO + hydrocarbons

These are believed to be minor pathways as experiments on deposition of Cu_2O from $Cu(hfac)_2$ and isotopically labeled $H_2^{18}O$ have shown that the oxygen in the deposited film arises mainly from $H_2^{18}O$ and not from the oxygen in the ligand molecule [41].

Recently, there have been a few experimental studies to determine the decomposition kinetics for the metal beta-diketonates. Most of the studies have been based on mass spectrometry where the concentration of the observed m/e peaks is followed to fit the data to an Arrhenius form for the overall decomposition process. The kinetic parameters obtained from these studies are summarized in table 3.

Precursor	Environment	Pre-exponential (1/sec)	Activation Energy (Kcal/mol)	Reference
$Cu(dpm)_2$	vacuum	1.5×10^{13}	$37.2 \; \forall \; 1.6$	[39]
$Cu(dpm)_2$	vacuum	1.5×10^{9}	27.0	[42]
	O_2	9.6×10^{11}	32.7	
$Cu(acac)_2$	vacuum	1.1×10^{8}	17.6	[42]
	H_2	1.2×10^{13}	31.8	
	O_2	7.2×10^{7}	17.2	
$Cu(acac)_2$	vacuum	3.0×10^{7}	27.5	[43]

Table 3. Kinetic parameters of the gas-phase pyrolysis of Cu (β–diketonates).

The reported values are observed to differ widely from each other. Also, the kinetic parameters are based on mass-spectrometric studies may not be able to capture the actual decomposition process which is believed to occur via a radical mechanism.

In light of the conflicting values reported in the literature, quantum chemistry studies can be used to determine the kinetic parameters. The rate-determining step for both $Cu(acac)_2$ and $Cu(dpm)_2$ decomposition appears to be the Cu-O bond break-up. This step is assumed to occur without a transition state. Based on the quantum chemistry calculations for the copper diketonates with the bidentate and the monodentate ligands, the activation energy for this step is ~ 27.0 kcal/mol. Pre-exponentials for this type of reactions range from 10^{13} to 10^{14}. The value of the pre-exponential of 10^{13} seems reasonable. These parameters can be used in the finite element simulations to model the CVD deposition of the HTS thin films.

Decomposition in the Presence of Oxygen:

The effect of oxidant gas such as oxygen on the decomposition of the Cu β-diketonates was also investigated. Oxygen binds to the $Cu(opo)_2$ precursor, forming a hexa-coordinated complex as shown in Figure 4. This is accompanied by the weakening of the Cu-O bond between the central copper atom and the oxygen atom from the ligand. The bond length between Cu-O increases from 1.94 Å in $Cu(opo)_2$ to 2.14 Å in $Cu(opo)_2.O_2$, which is indicative of the weaker Cu-O (ligand) bond. $Cu(opo)_2$ has the H atoms as substituents on the ligand. It is possible that such a structure is unstable and falls apart easily. It seems that oxygen reacts with the metal directly forming CuO_2 and CuO.

In several deposition studies, where $Cu(hfac)_2$ is employed as a copper precursor, water vapor is used along with O_2 as the oxidant. Quantum chemistry calculations show the tendency of a $Cu(hfac)_2$ to bind to the oxygen of the water to form a penta-coordinated complex. This tendency of flourinated copper precursors to coordinate an nucleophillic nucleus, such as O in

21

H_2O, to form higher coordinated compounds has also been observed experimentally, where a water molecule was shown to bind to the Cu atom of $Cu(hfac)_2$ [41, 44]. Recent experiments on deposition of Cu_2O from $Cu(hfac)_2$ and isotopically labeled $H_2^{18}O$ have shown that the oxygen in the deposited film arises mainly from $H_2^{18}O$ and not from the oxygen in the ligand molecule [41].
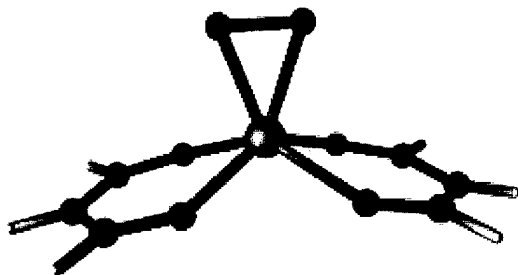
Figure 8. Optimized structure of the $Cu(opo)_2$-O_2. Coordination with O_2 increases the Cu-O (ligand) bond distance.
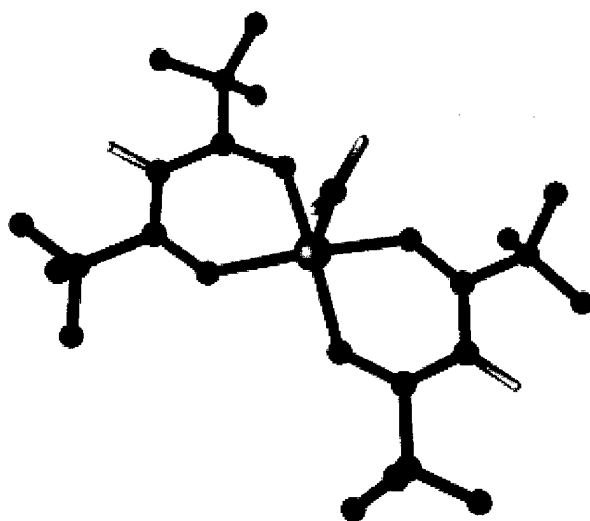
Figure 9. Optimized structure of the $Cu(hfac)_2$-H_2O.

2. Yttrium Precursors:

Yttrium tris(dipivaloylmethante) or $Y(dpm)_3$ is the most common precursor employed for deposition of yttrium containing HTS films. The large number of electrons present in Y along with the bulky t-butyl ligands makes the task of studying this molecule quite challenging. ONIOM calculations were done to obtain the structure of $Y(dpm)_3$ and compared with the structure for $Y(acac)_3$, where the t-butyl groups have been replaced by CH_3.
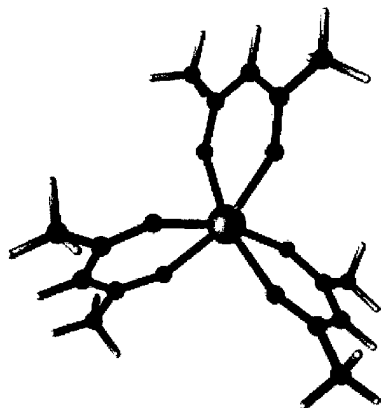
Figure 10. Optimized structure of the Y(acac)₃.

Y(acac)₃ was chosen as a model for Y(dpm)₃ and bond dissociation energies were calculated for the Y-O bond. The bond dissociation energy for the removal of the first ligand from Y(acac)₃ according to the reaction

$$Y(acac)_3 \rightarrow Y(acac)_2 + acac$$
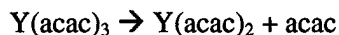
is 61 kcal/mol. The mean bond dissociation energy for the Y-O in Y(dpm)₃ is 68 kcal/mol. The initial step is the decomposition of Y(dpm)₃ is the splitting of the bulky t-butyl ligand. The loss of t-butyl from the ligand causes the Y-O bond to weaken. This weakening of the bond causes the ligand to be split-off from the molecule resulting in Y(dpm)₂ which is more stable compared to the parent molecule, Y(dpm)₃. This is evidenced from the shortening of the Y-O bond in Y(dpm)₂ and Y(acac)₂ as compared to the Y(dpm)₃ and Y(acac)₃. Y(dpm)₂ has been detected as a stable species in the gas phase at temperatures as high as 760 K [33, 45].

Two different structures were obtained for Y(acac)₂. In structure I, Y is square-planar coordinated, and in structure II, Y is in tetrahedral coordination. The two structures are shown in figure 11. A planar structure has also been predicted for Y(dpm)₂ based on electron diffraction data [33]. Quantum chemistry calculations predict the tetrahedral structure to be more stable compared to the planar structure by 38 kcal/mol.

23
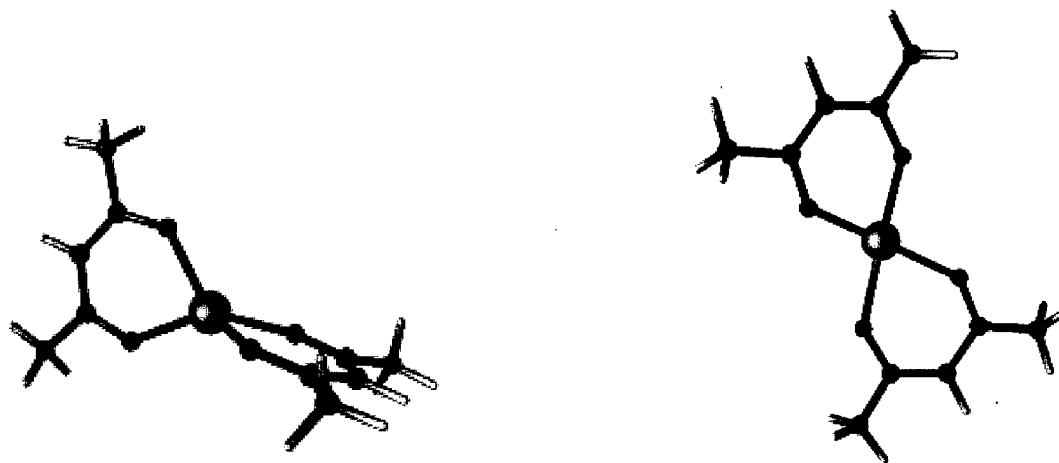
Figure 11. Optimized structures for Y(acac)$_2$.

A kinetic mechanism for decomposition of Y(dpm)$_3$ based on the above observations is:

Y(dpm)$_3$ $\rightarrow$ (Y(dpm)$_3$ – C$_4$H$_9$) + C$_4$H$_9$

Y(dpm)$_3$ $\rightarrow$ (Y(dpm)$_3$ – 3 C$_4$H$_9$) + 3 C$_4$H$_9$

(Y(dpm)$_3$ – C$_4$H$_9$) $\rightarrow$ Y(dpm)$_2$ + C$_4$H$_9$ + (CO)CH(CO)

Y(dpm)2 $\rightarrow$ Y + 2 dpm

4 Y + 3 O$_2$ $\rightarrow$ 2 Y$_2$O$_3$
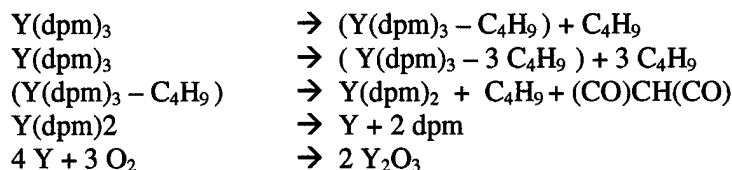
Conclusion on CVD Kinetics Modeling

We have developed a systematic methodology to look at the structure and reactivity of the metal β-diketonates precursors, used in the chemical vapor deposition of high temperature superconductors, using first principle quantum chemistry methods. The large size of the precursor molecules has so far limited studies of this nature. Very little information is available on the chemistry of these compounds. Semi-empirical methods were found inadequate in describing the structures and traditional ab-initio methods were deemed to be very expensive, given the size of the molecules. We have tested and validated different density functionals for describing these molecules. Based on our validations, an effective core potential was chosen to describe the metal (Cu and Y). We have investigated the decomposition mechanism for Cu(acac)$_2$ and Cu(dpm)$_2$, two of the most common precursors for copper in HTS films. A kinetic mechanism for decomposition was formulated and the initial break-up of the Cu-O bond was determined to be the rate-limiting step. A similar investigation was also carried out for Y(acac)$_2$, which serves as a model for Y(dpm)$_3$. A preliminary mechanism has been put together based on the work done so far.

3. Reactor Scale Modeling of MOCVD of HTS

The objective of this work is to develop a detailed and accurate reactor-scale, physical model that predicts deposition rate and stoichiometry along the wafer surface when the operating conditions and inflow gas composition are specified. The physical model has to address precursor decomposition and oxide formation chemistry, and the transport processes (fluid mechanics, species diffusion, and heat transfer) associated with CVD. The reactor modeled here is the Thomas Swan reactor used by STI for their production of YBCO superconducting thin films (HTS). For modeling chemistry, we have used kinetics data developed from quantum chemistry calculations described earlier, supplemented by other data in the literature.

A detailed description of various aspects of non-metal CVD is the subject of a recent book [59]. Various reactor configurations such as planetary, barrel, and pancake reactors for MOCVD are described in [60]. The more specific topic of MOCVD of high-T_c HTS is discussed in two excellent review papers [61, 62], and there are several reports of experimental results in the literature, e.g., [67,68].

MOCVD of HTS materials is a relatively new area of research, and there is little published on reactor-scale simulation for comparison with our work. Hence, a step-by-step approach towards acquiring capability for reliable MOCVD simulations was adopted in this study. The first step was to perform simple CVD calculations with one-step, finite-rate chemistry for the above 2-D reactor and compare with results in the literature. The case studied was silicon epitaxy using trichlorosilane (SiHCl$_3$), and the detailed problem was identical to that solved by the Habuka *et al* [52]. A commercial software package, CFD-ACE [63], popular in the semiconductor industry, was used for our modeling work. The equations solved by CFD-ACE to calculate CVD deposition rates are described next using the silicon epitaxy example, followed by the detailed validation problem before describing MOCVD of HTS.

Equations of CVD

The global CVD reaction for deposition of epitaxial silicon at the surface of the wafer is represented by:

$$SiHCl_3 + H_2 \rightarrow Si + 3 HCl$$
$$\text{(gas)} \quad \text{(gas)} \quad \text{(solid)} \quad \text{(gas)}$$
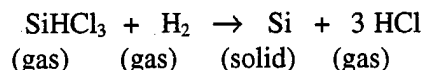
An Arhennius-type kinetic rate constant, k, for the global one-step reaction was obtained from Habuka *et al* [5] as:

$$k = 2650 \exp \frac{-138,000}{RT} \; ; (units: m^4 /(gm - mole.s))$$

Here, T is the temperature in Kelvin, k_B is the Boltzman constant. The deposition rate is then obtained using

$$d = k[SiHCl_3] \, [H]$$

Here, the quantities in square brackets are molar concentrations, d is the deposition rate in

moles/m^2/s. The equations that are solved using CFD-ACE are the mass, momentum, energy, and species concentration equations. The mass conservation (continuity) equation has the following form:

$$\frac{\partial \rho}{\partial t} + \frac{\partial}{\partial x_j}\left(\rho u_j\right) = 0$$

The mixture density, ρ, depends on temperature, and is computed using the ideal gas law. The first term in this and the following equations represent time-dependence of the quantities. Although all the flow and temperature fields are steady-state, the term is included here for completeness. The term u_j is the jth component of the instantaneous velocity. The momentum conservation equations, or the Navier-Stokes equations have the following form:

$$\frac{\partial}{\partial t}\left(\rho u_i\right) + \frac{\partial}{\partial x_j}\left(\rho u_i u_j\right) = -\frac{\partial p}{\partial x_i} + \frac{\partial}{\partial x_j}\left[\mu\left(\frac{\partial u_i}{\partial x_j} + \frac{\partial u_j}{\partial x_i}\right) - \frac{2}{3}\mu\frac{\partial u_k}{\partial x_k}\delta_{ij}\right] + \rho f_i$$

In the above equation, p is the static pressure, f_i is the body force, and δ_{ij} is the Kronecker-delta function. The mixture viscosity, μ, is also temperature dependent. The three momentum equations yield the three Cartesian components of velocity. The energy balance equation is written in terms of the enthalpy, h (static enthalpy for these relatively low speed flows), as follows:

$$\frac{\partial}{\partial t}\left(\rho h\right) + \frac{\partial}{\partial x_j}\left(\rho u_j h\right) = -\frac{\partial q_j}{\partial x_j} + \frac{\partial p}{\partial t} + u_j\frac{\partial p}{\partial x_j} + \tau_{ij}\frac{\partial u_i}{\partial x_j} - u_j\frac{\partial(J_i h_i)}{\partial x_j} + S_a$$

The last term on the right side represents viscous dissipation, and is not considered in our calculations because it is very small at these low velocities. The second term on the left hand side is the enthalpy convection term. The first term on the right hand side represents conduction heat flux, which is modeled using Fourier's law. Replacing the temperature variable, T, by h using $h = c_p T$, where c_p is the specific heat capacity, this term takes the following form:

$$q_j = -\frac{k_T}{c_p}\frac{\partial T}{\partial x_j}$$

Here, k_T is the thermal conductivity of the gas. The species transport equation has the following form

$$\frac{\partial}{\partial t}\left(\rho \omega_i\right) + \frac{\partial}{\partial x_j}\left(\rho u_j \omega_i\right) = \frac{\partial J_i}{\partial x_j} + S_i$$

The term ω_i is the mass fraction of the ith species, J_i is its diffusive mass flux, and S_i is a volumetric source term representing creation or consumption of the ith species *via* chemical reaction. Since the CVD problem here is solved as a surface reaction, $S_i = 0$. The above equation is solved for any two of the three gaseous species, and the third mass fraction is obtained by subtracting the sum of the rest from unity. The diffusive mass flux, J_i, is the sum of the flux driven by concentration gradient , J_i^C, and the thermodiffusive (Soret) flux, J_i^T, driven by temperature gradient. The concentration diffusive flux for any species depends on the mass concentration gradients of *all* the species through the Stefan-Maxwell equations [67] shown below:

$$\frac{\partial \omega_i}{\partial x_j} + \omega_i \frac{\partial}{\partial x_j}\left(\ln \overline{M}\right) = \sum_{k \neq i}^{N} \frac{\overline{M}}{\rho D_{ik}} \frac{\omega_i J_k^c}{M_k} - \frac{\omega_k J_i^c}{M_i}$$

Here, D_{ik}, is the binary diffusion coefficient of species i with respect to species k. M_i is the molecular weight of species i, $\overline{M}$ is the average molecular weight of the gas, and N is the total number of species. The above equation is solved iteratively to yield J_i^C as a function of the various mass fractions subject to the following constraint.

$$\sum_{i=1}^{N} J_i^c = 0$$

The Soret diffusion flux, which drives the gas away from hot walls towards cooler walls, is given by

$$J_i^T = D_i^T \frac{\partial}{\partial x_j}\left(\ln T\right)$$

Here, D_i^T is the thermodiffusive coefficient. As stated earlier, the temporal terms in all the above equations are neglected in the calculations. This pseudo-steady-state condition is justified because the time scales of transport are much shorter (of the order of a few seconds) than the time scales for film growth, especially at lower pressures. The boundary condition for the species equation at the deposition surface is obtained by balancing the sum of the advective and diffusive fluxes of the species normal to the wall against the flux of species generated (or consumed):

$$\left(\vec{V}(\rho \omega_i) + J_i\right) \cdot \hat{n} + M_i \sum_{l=1}^{nr} d_{il} = 0$$

Here, $\vec{V}$ is the velocity vector, n is the normal to the surface, nr is the total number of surface reactions, and d_{il} is the molar flux of species i generated (or consumed) in reaction l.

The above transport equations are solved using a control-volume approach [63] for the structured grid. In this solution, a first-order upwind scheme was used for the convective fluxes. CFD-ACE uses a pressure-based approach to solving the Navier-Stokes equations in which the continuity equation is used to recast these three equations is terms of pressure. This solution used the SIMPLEC method, a variation of the well-established SIMPLE algorithm [64].

CVD validation studies for silicon epitaxy

Figure 12 shows the geometry used in the 2-D model obtained from Habuka *et al* [52]. The end-to-end length of the radiantly-heated chamber is 0.705 m and the total height is 0.4 m. The top part of the left wall and the entire right wall are at 300 K, and the sections of the top and the bottom wall immediately above the susceptor are at specified temperatures. The rest of the walls are adiabatic. The flow enters at atmospheric pressure from the top left corner of the chamber, and exits from the bottom right corner. The 8" wafer is located at the center of the 12" susceptor, 0.205 m from the left end of the chamber.

Gas in

IR Furnace

Quartz Glass Wall

Wafer

Susceptor

Gas out
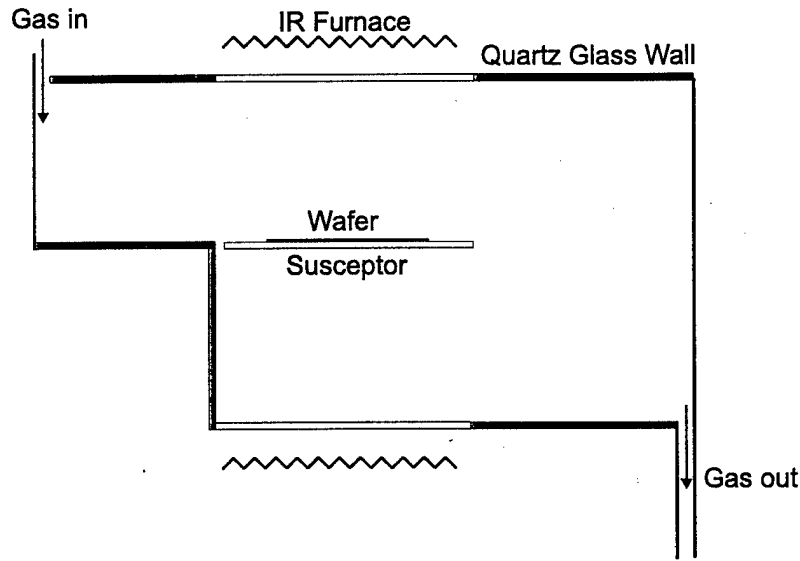
Figure 12. Schematic of a two-dimensional horizontal CVD reactor [52]. The figure is not to scale. Shaded walls are adiabatic. The part of the walls next to the IR heaters are semi-transparent and at elevated temperatures.

A gaseous mixture, consisting of trichlorosilane ($SiHCl_3$, nominal mass fraction=0.71) and hydrogen, is injected into the chamber at room temperature (300K) and a velocity of 0.67 m/s. The wafer temperature is isothermally elevated to a nominal value of 1423K. The temperatures of the hot sections of the top and bottom walls, T_{wall}, were measured by Habuka *et al* [52], and expressed as the following linear function of the susceptor temperature, T_{sus}:

$$T_{wall} = 730 + (770-730)(T_{sus}-1393)/(1453-1393)$$

For T_{sus} = 1423K, T_{wall} = 750K. The other sections on the top and the bottom walls are kept at 300K. The susceptor (and hence, the wafer) temperatures are assumed to be independently controlled to excellent uniformity.
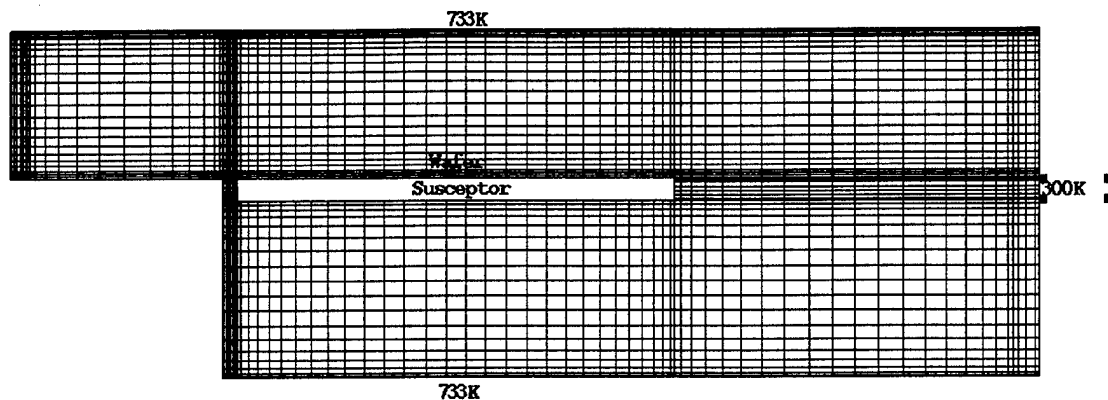
Figure 13. Mesh for numerical solution using CFD-ACE. The 90 X 53 mesh (with 3399 cells or control volumes in all) is clustered near the walls and near regions of high temperature gradients at the edges of the wafer. For clarity, the vertical dimensions are magnified five times the horizontal dimensions.

Figure 13 shows the mesh generated for the control-volume solution. The solution converged after 600 iterations in about half-an-hour on a Pentium PC. Figure 14 shows the velocity vectors with superposed temperatures for nominal conditions (trichlor mass fraction of 0.71, wafer temperature of 1423K, and top and bottom quartz wall temperatures of 750K). The gas is heated up considerably by the susceptor and the wall, and speeds up along the wafer surface. Figure 15 shows comparison of deposition rate uniformity with Habuka *et al* [52]. Figure 16 shows that wafer rotation significantly improves deposition uniformity, assuming that the rotation period is much smaller than the deposition period (which is almost always the case). The CFD-ACE results compares quite well with those Habuka *et al* [52], the average deposition rate difference being about 10%.
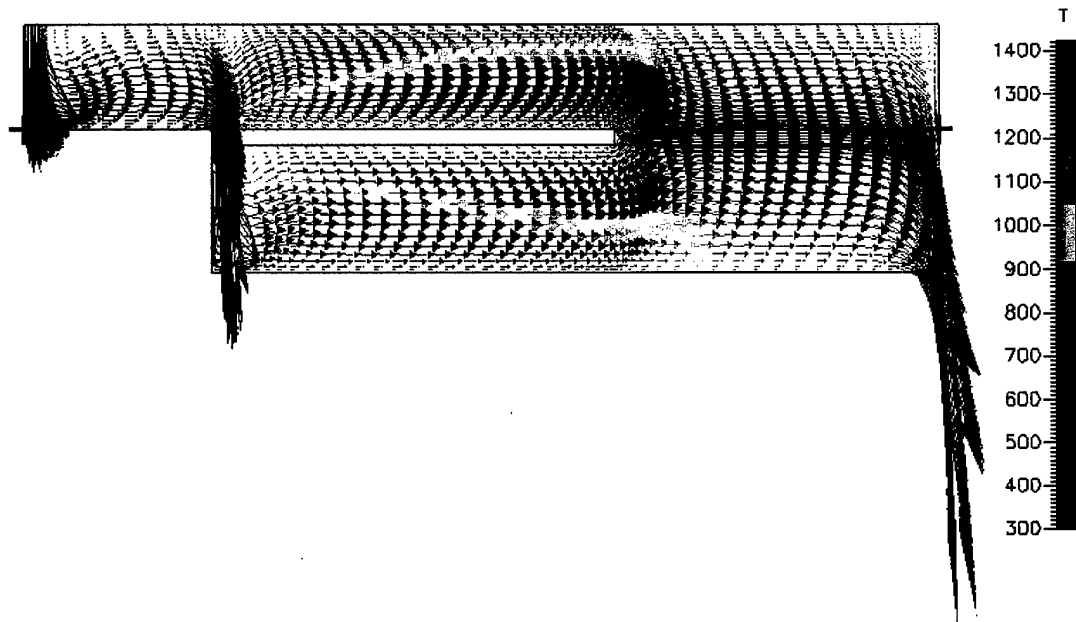
Figure 14. Gas velocity vectors with superposed temperature.
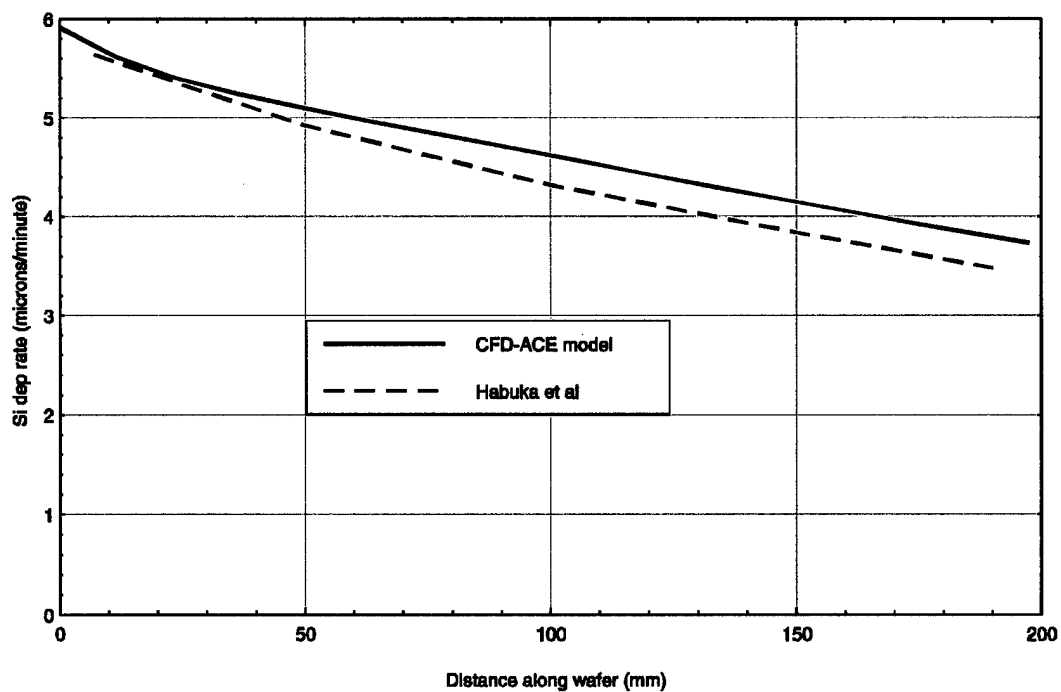
Figure 15. Deposition profile along flow direction. Comparison with Habuka, *et al* [52].

30
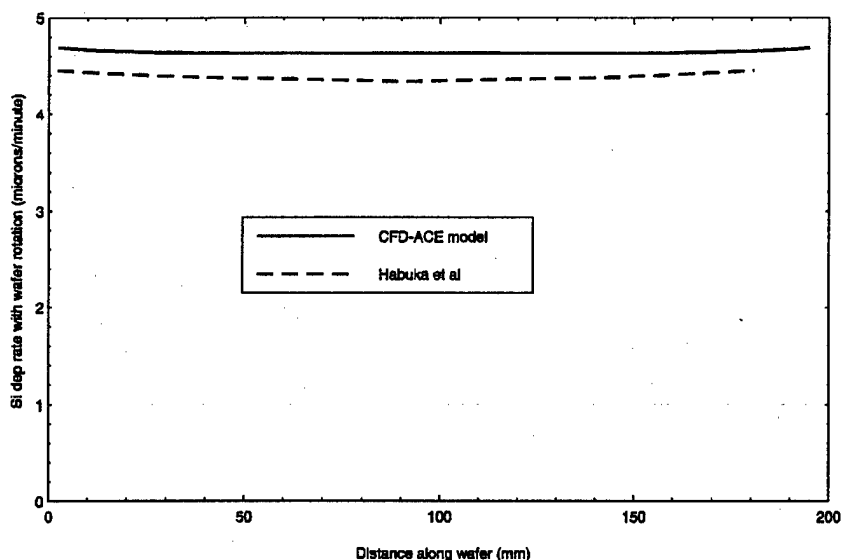
Figure 16. Effect of wafer rotation on deposition rate uniformity.

The deposition rates were calculated by varying the trichlor mass fraction. The results are plotted in Figure 17. These results agree well with Habuka's experimental data. The slight over-prediction of the deposition rate may be attributed be due to two possible causes. First, the temperatures at the adiabatic parts of the wall are relatively high, and in reality, there is probably some deposition on the walls leading to reactant depletion downstream. Second, there is always a small amount of HCL etching of deposited silicon that reduces the overall deposition rate.
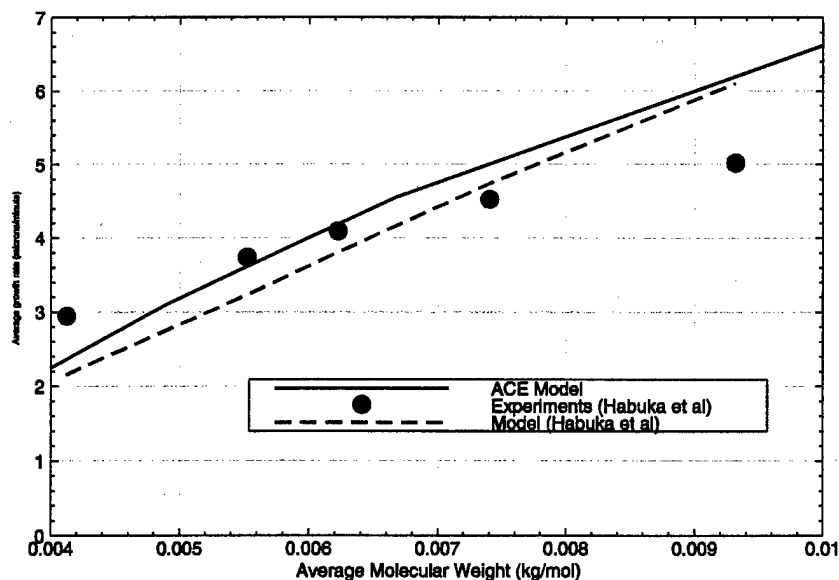
Figure 17. Average deposition rate as function of average molecular weight of gas at inlet. Nominal molecular weight is 6.67 kg/kg-mole (when trichlor mass fraction = 0.71).

Several tests were carried out on the model to establish convergence on the basis of mesh refinement and number of iterations needed. The results are shown in Figure 18. We find that reducing iterations from 5000 to 1000 results in an average difference of 0.5% in the deposition

31

rate. Based on this result, it is arbitrarily decided that for this geometry, 1500 iterations are sufficient. Reducing the number of cells from 3399 to 1381 changed the average deposition rate by 0.8%, and the average horizontal centerline temperature by 0.7%. Hence, 1381 cells are deemed sufficient. It is also noted that the time per iteration rises non-linearly for more refined mesh, which is to be expected from this solver.

From this validation study, we concluded that the results for a simple CVD model agree well with those published in the literature, giving us the necessary confidence to proceed with modeling of MOCVD of YBCO thin films.
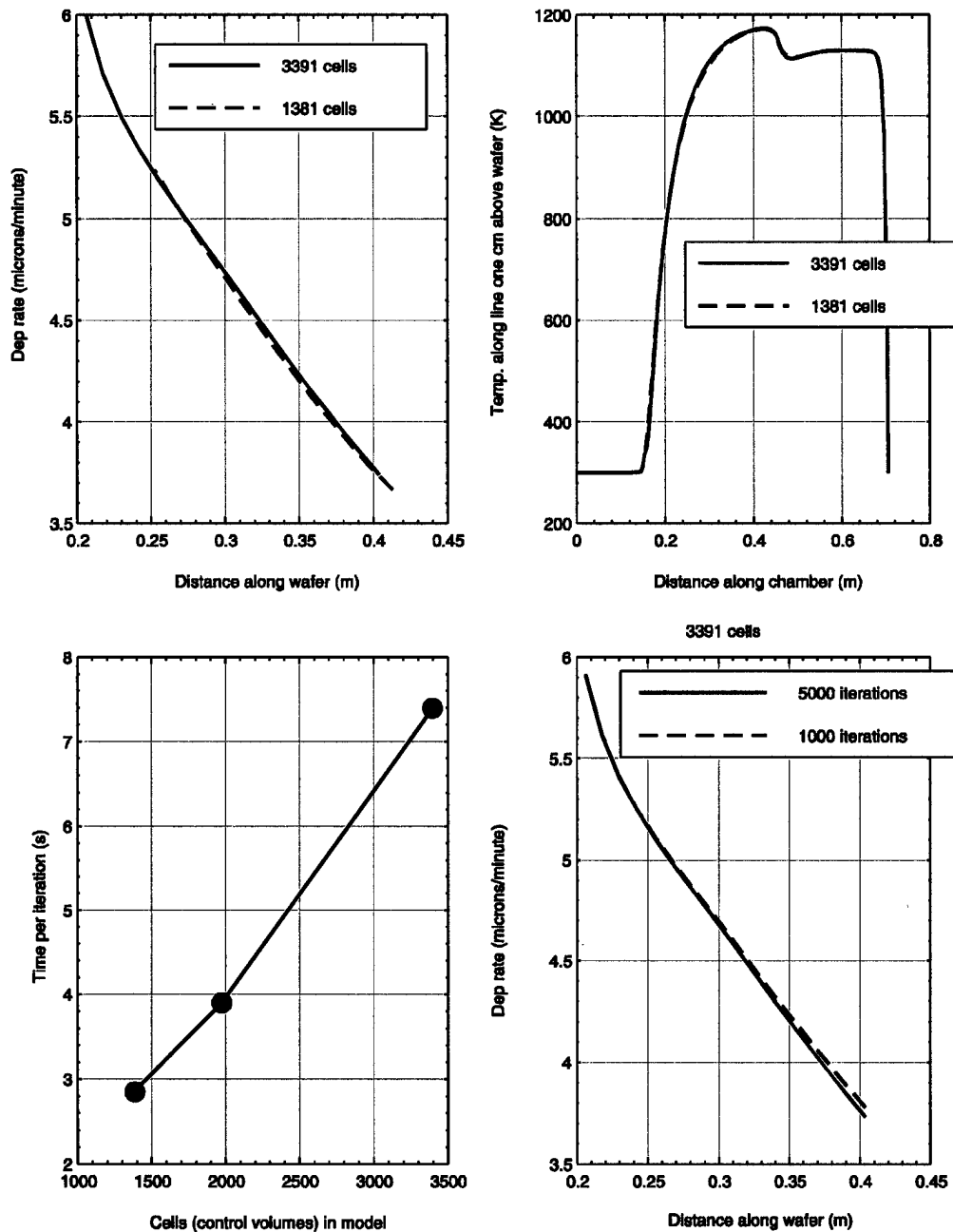
Figure 18 Convergence study using deposition rates and gas temperatures.

32

Physical Model for MOCVD of HTS

A 2-D version of the geometry of the commercial, hot wall reactor (Thomas Swan) used at STI was developed for modeling MOCVD of HTS. The reactor is infinite in the transverse direction and is shown in Figure 19. The center of the wafer of diameter 2" is located 20 cm from the left end of the reactor through which the gas mixture enters. The ceiling of the reactor slopes downward in order to increase species concentration gradients in the vertical direction, which in turn increases species flux towards the wafer surface. This design thus improves deposition uniformity by compensating for species depletion along the wafer caused by deposition.
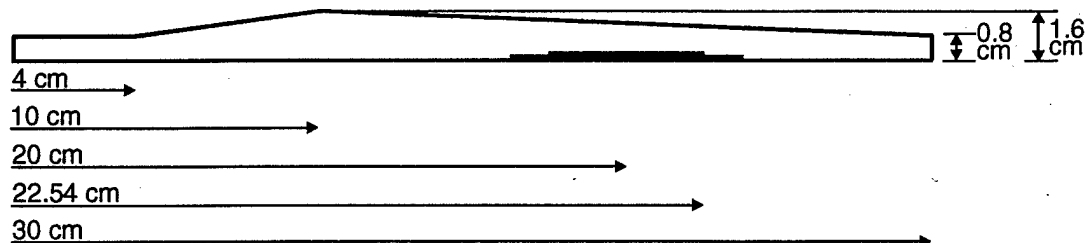
Figure 19. Schematic of STI's Thomas Swan MOCVD reactor.

Figure 20 shows the structured mesh constructed for the above reactor, magnified five times in the vertical direction for clarity. The mesh consists of 574 (14×41) cells which was found sufficient for obtaining a converged solution.
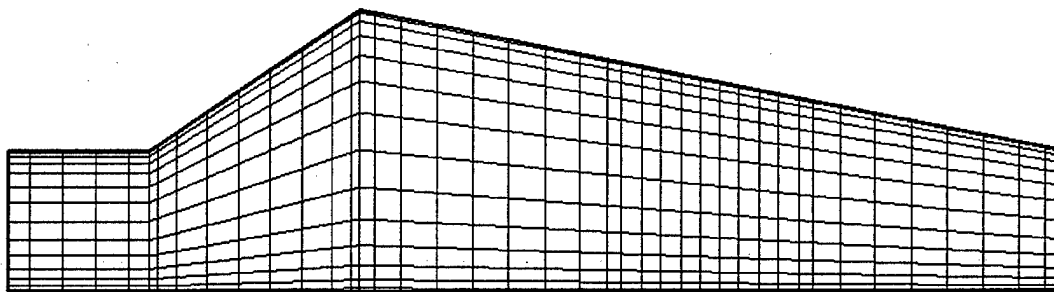
Figure 20. Mesh for numerical solution using CFD-ACE, clustered near the walls. For clarity, the vertical dimensions are magnified five times the horizontal dimensions.

For chemistry, we have used one-step global mechanisms for precursor decomposition. For Cu(dpm)$_3$, the kinetic rate constants were obtained from quantum-mechanical calculations performed in this program. For the other two precursors, the kinetic mechanism were obtained from the Colorado School of Mines [53], another VIP program participant. They derived the `global' empirical mechanism from existing literature. The overall mechanism consists of seven gas phase reactions:

$$Y(dpm)_3 + O_2 \rightarrow Y + 3 (dpm) + O_2$$

$$Y(dpm)_3 \rightarrow Y + 3 (dpm)$$

$$Cu(dpm)_2 \rightarrow Cu + 2 (dpm)$$

$$Ba(dpm)_2 \rightarrow Ba + 2 (dpm)$$

$$4 Y + 3 O_2 \rightarrow 2Y_2O_3$$

$$2 Ba + O_2 \rightarrow 2BaO$$

$$2 Cu + O_2 \rightarrow 2CuO$$
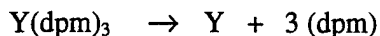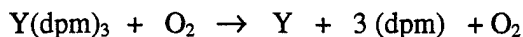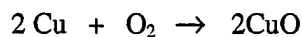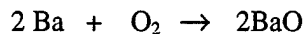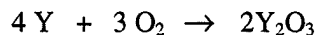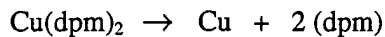
The last three oxidation reactions are relatively fast. The Arrhenius rate constants for the first four reactions are as follows. The pre-exponential terms for the four reactions are 5.9×10^{-12} m^3/kg-mole.s, 2.2×10^9 s^{-1}, 1.0×10^{13} s^{-1}, and 2.2×10^9 s^{-1}, respectively. The characteristic temperature (E_a/R) are 13590.4 K, 17264.9 K, 13620.6 K, and 17264.9 K, respectively.

The oxides produced in the gas phase reaction diffuse to the surface and their deposition was modeled using sticking coefficients. Since the transport is diffusion limited, choice of sticking coefficient is not critical. This issue is discussed later in the section. Sticking coefficients of unity were used for all three oxide species. The transport properties of some of the species were calculated using Lennard-Jones parameters. For the oxides, data on melting point temperatures, T_m [65], and the liquid molar volume, V_b, were used to calculate the parameters using the following correlations from the literature [65].

$$\varepsilon/k = 1.92\, T_m; \sigma = 1.166\, V_b^{1/3}$$

For the precursors, melting point data was used to calculate ε/k. The collision diameter, σ, was calculated from data on σ_{ij} for precursor and oxygen [66]. Since data for $Cu(acac)_2$ is reported, we use these values for $Cu(dpm)_2$ for lack of more accurate values of the transport properties. Finally, the values of Lennard-Jones parameters used in the model are tabulated below.

Species	Melting pt (K)	ε/k_B (K)	σ (A)
Y(thd)3	523	601	17.7
Ba(thd)2	606	697	15.3
Cu(thd)2	625	719	10.8
thd		272	9.38
Y2O3	2410	4627	4.35
BaO	1918	3683	3.66
CuO	1326	2546	2.83

The oxidation reactions are instantaneous while the decomposition reactions are finite-rate, make the system of equations very stiff. We decided to simplify the model by eliminating the four oxidation reactions. The metallic atoms are assigned the transport properties of the oxides, which then diffuse to the surface. Because the mole fractions of the precursors are very small (of the order of tens of ppm), the excess oxygen not used up in oxide formation are also very small, and its effect on the flow and temperature fields is insignificant. This simplification halved the computational time without any loss in accuracy. A further saving of 25% in simulation time was achieved by neglecting Soret diffusion (thermodiffusion) and Stefan-Maxwell conservation.

Because the temperature gradients inside the reactor are small, Soret diffusion was found to be negligible. The concentrations of the three oxides are very small. Hence, neglecting Stefan-Maxwell conservation for multi-species diffusion caused negligible error in the deposition rate. A typical simulation would converge within 1200 iterations in approximately two hours of CPU time on Pentium PC.

Results are shown below for the following representative steady-state operating conditions [53]. The precursors are well mixed with oxygen, nitrogen, and argon and enter the reactor at 10 Torr at a velocity of 2 m/s and temperature of 513K. The inlet mass fractions are: $O_2=0.456$, $N_2=0.422$, Ar=0.114, $Y(dpm)_3=9.32\times10^{-4}$, $Ba(dpm)_2=1.57\times10^{-3}$, $Cu(dpm)_2=5.02\times10^{-3}$. The wall of the plenum is insulated up to the highest point of the chamber (10 cm from the entry port). The remaining 20 cm of the reactor are heated radiantly so that both the top and bottom surfaces are kept at 1073K. Although the 2" diameter wafer is centered 20 cm from the entry port, deposition occurs along the entire length of the heated lower surface. Figure 21 shows the flow velocity vectors with the color scheme showing the magnitude (speed). The flow speeds up considerably as it gets hotter. Figure 22 shows the temperature contours, and Figure 23 shows the Y_2O_3 mass fraction contours.

In this model, YBCO deposition rate is calculated by adding the deposition rates of each of the three individual oxides.
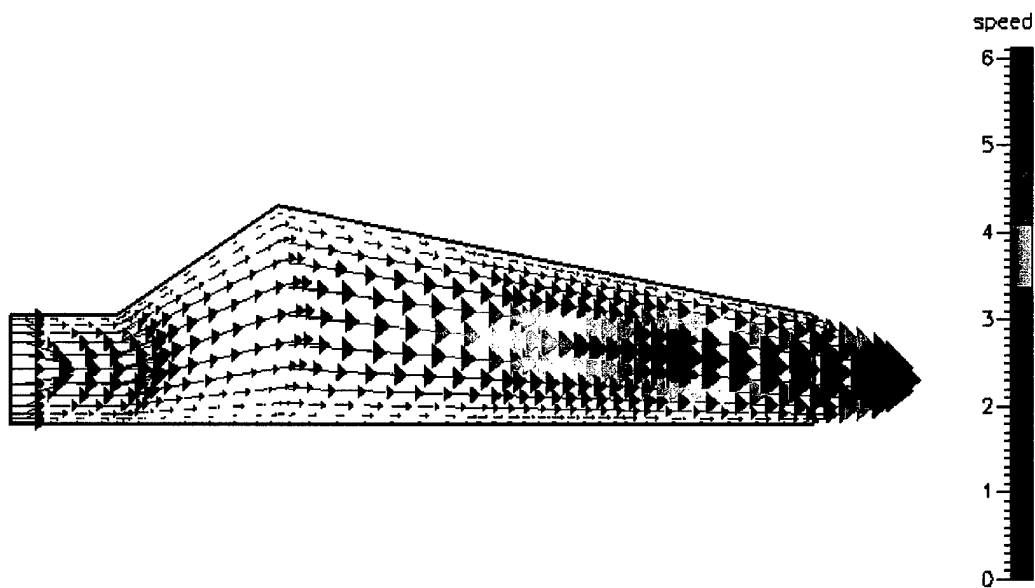
Figure 21. Velocity distribution in MOCVD reactor.
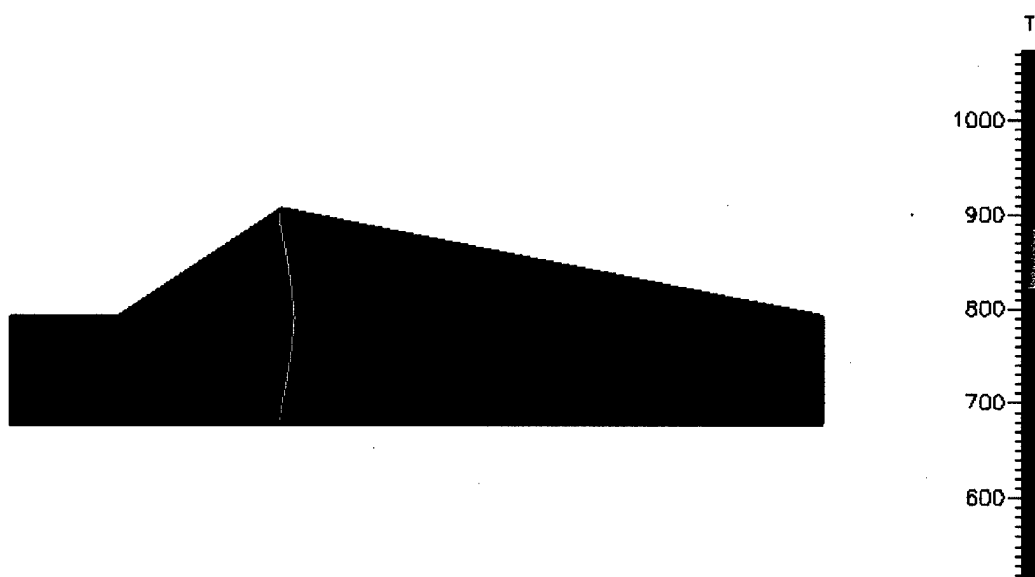
Figure 22. Gas temperature distribution within the MOCVD reactor.
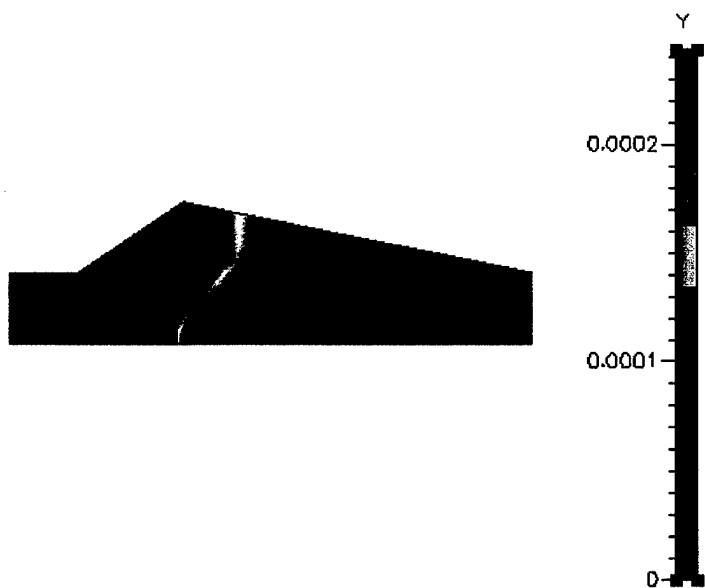
Figure 23. Yttrium oxide mass fraction distribution in reactor.

Figure 24 shows the precursor concentrations along the reactor length 5 mm above the wafer surface, and also the oxide concentrations across the height reactor at the center of the wafer. It is seen that the precursors decompose very quickly as they enter the heated region.
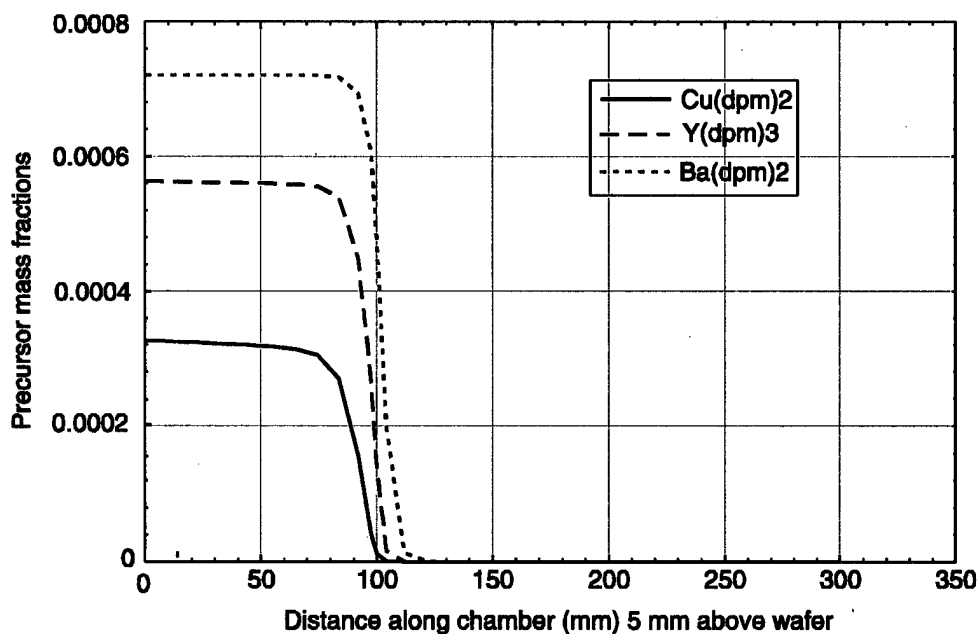
Figure 24. Spatial profiles of various species along reactor length.
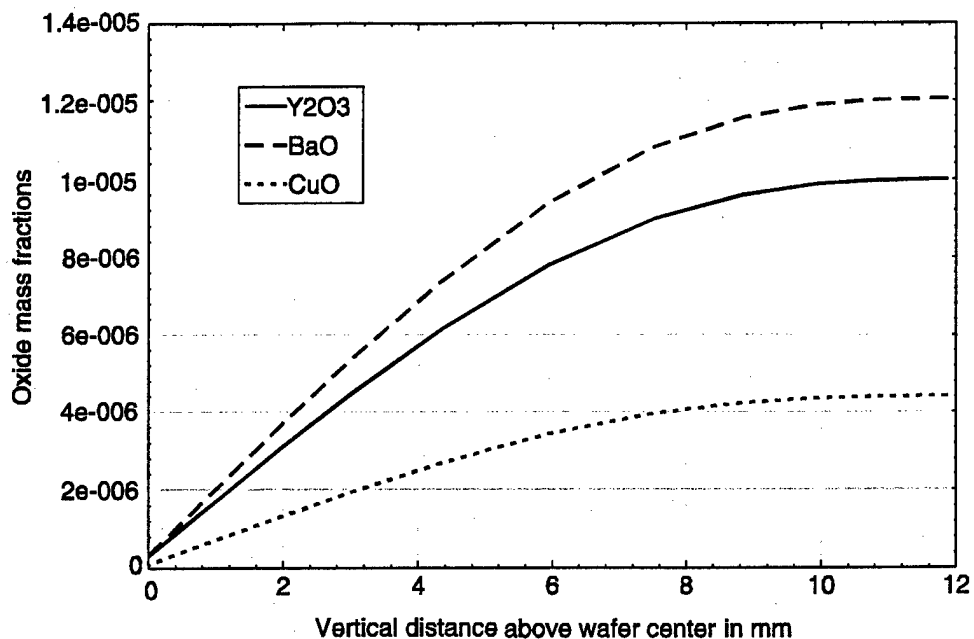
Figure 25. Spatial profiles of various species in the vertical direction.

Figure 25 shows the oxide mass fractions in the vertical at the center of the wafer. The oxides concentrations are very small near the surface because of depletion due to deposition.
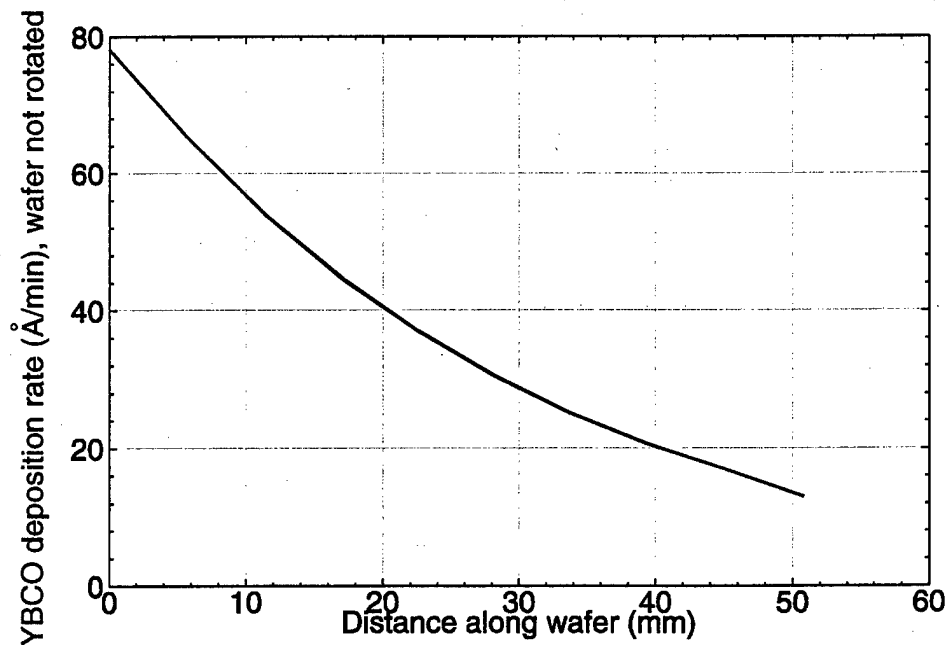
Figure 26. YBCO deposition rates in Angstroms/minute, wafer not being rotated.

38
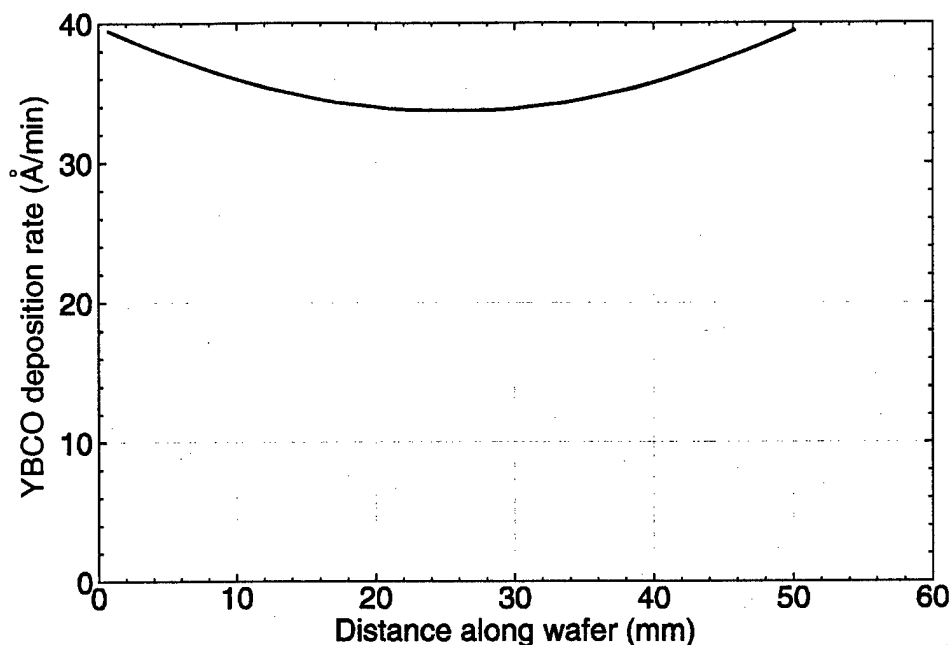
Figure 27. YBCO deposition rates in Angstroms/minute, wafer rotated.

Figure 26 shows the deposition rate along the diameter of the 2" wafer for the case where the wafer is static, while Figure 27 shows deposition uniformity when the wafer is rotated. Although the deposition occurs more uniformly with wafer rotation, the 20% non-uniformity within a 2" wafer is still rather high. The average deposition rates of 35.7 Å/min are in the range of 30-40 Å/min deposition rate obtained by STI.

Earlier it was stated that the deposition process is transport limited. Figure 28 shows that this is indeed the case, with deposition rate of yttrium oxide showing little change with a five-fold increase in sticking coefficient. Deposition on the entire heated substrate, rather than just the 2" wafer, is shown in this graph. Figure 29 shows the stoichiometry of YBCO thin film across the wafer. The stoichiometry changes from point-to-point. In general, its is desirable to have the BaO/Y_2O_3 ratio slightly below two, and the CuO/Y_2O_3 ratio slightly above three [62].

39
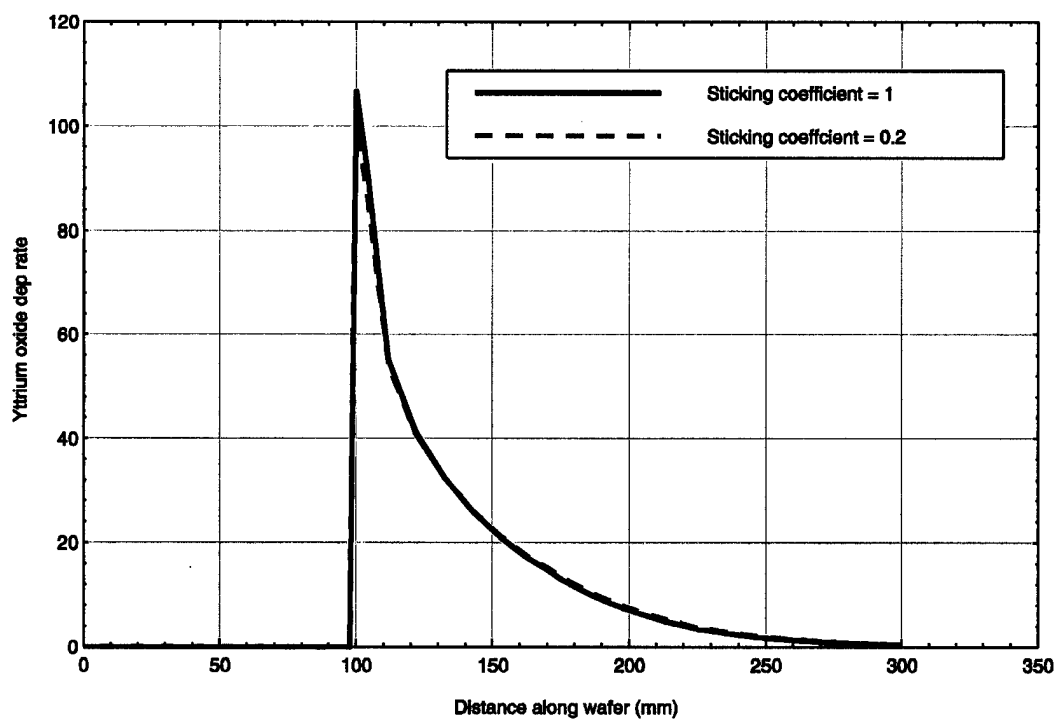
Figure 28. Effect of choice of sticking coefficient on Y_2O_3 deposition rate.
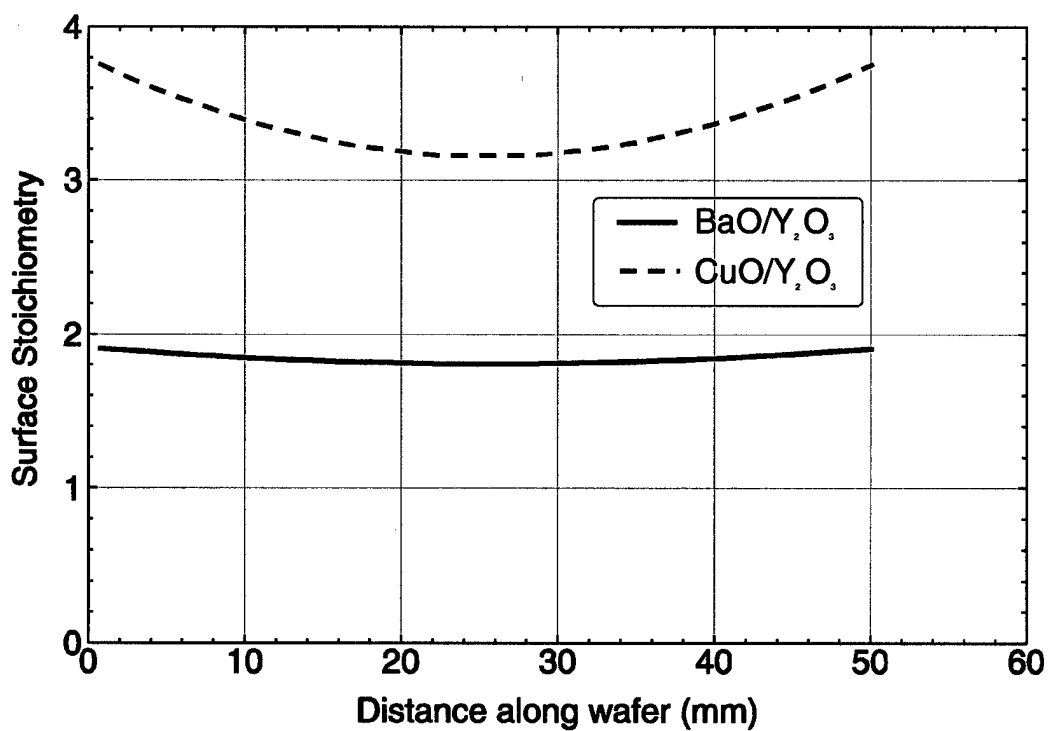
Figure 29. Oxide stoichiometry at wafer surface.

4. POD-Galerkin for Chemistry Reduction

The motivation for this research stems from the need to develop reduced models of chemistry in reacting flow problems. The numerical solution of such problems, where the right-hand-side is complicated by the presence of homogeneous chemical reaction, can be difficult and computationally expensive. Convergence of the numerical solutions can become even stiffer in the case of heterogeneous chemical reactions, which introduce highly nonlinear boundary conditions to the sets of nonlinear PDEs whose solution is desired; examples include catalytic combustion as well as crystal growth by CVD. The complexity of the chemistry clearly increases with the number of gas-phase and surface species involved in the reactions. It is therefore understandable that in reacting flows the reduction of the chemistry to a few components (pseudospecies) will not only improve the speed of the solution by decreasing the number of equations to be solved, but will also, especially in the case of complex heterogeneous reactions, dramatically improve convergence.

The Proper Orthogonal Decomposition (POD) method was used for chemistry reduction. While PODs have been used before for reducing the order of various transport fields (temperature, velocity), the parallel *individual* reduction of chemistry was the issue we needed to investigate. A comparison with the simultaneous construction of PODs from all transport and chemistry fields needs to be also constructed in also to assess the effectiveness of the technique.

POD-based compression of two kinetic schemes were considered; the first, describing the MOCVD growth of Si from $SiCl_2H_2$ using H_2 as the carrier gas, and the second describing Si deposition kinetic mechanism in the $SiCl_2H_2$ / B_2H_6 / H_2 system. As a first step we examined the POD content of the concentration dynamics and of the temperature dependence of a subset of the first reaction mechanism. For this purpose the gas-phase reaction mechanism was considered separately. This scheme involves 5 gaseous species and 6 chemical reactions; namely:

$$1. \ SiCl_2H_2 \ \text{-->} \ SiCl_2 + H_2$$
$$2. \ SiCl_2 + H_2 \ \text{-->} \ SiCl_2H_2$$
$$3. \ SiCl_2 + H_2 \text{-->} \ HSiCl + HCl$$
$$4. \ HSiCl + HCl \ \text{-->} \ SiCl_2 + H_2$$
$$5. \ SiCl_2H_2 \ \text{-->} \ HSiCl + HCl$$
$$6. \ HSiCl + HCl \ \text{-->} \ SiCl_2H_2$$

An "effective" batch reactor chemistry was taken into account and the corresponding system of ODE's was constructed. The concentration curves of $SiCl_2H_2$ from the time-integration are shown in Figure 30 (solid lines) for 3 different temperatures T=950,1100 and 1200 K and an operating pressure of 1 atm. A data ensemble of time-dependent concentration curves of the 5 gaseous species for the 3 different temperatures was considered and the eigenvalues of the two-point correlation matrix revealed that one mode captures 99.99% of the system's energy. The projections of the transient evolution of $SiCl_2H_2$ concentration (obtained from the ODE model) on the corresponding eigenfunction are depicted in Figure 30 (dashed lines). As can be seen both the transient concentrations and the steady states at different temperatures are accurately captured. This is an indication that the kinetic mechanism of the Si deposition system can be successfully reduced via the POD method.

Initial results for the Galerkin projection of these ODEs on the POD modes indicate that the short-term dynamics are accurately captured, but show deviations for the long-term dynamics. As the research concludes, we are studying the possibility of creating a richer data ensemble, perturbing the data in directions orthogonal to the most important POD vectors.
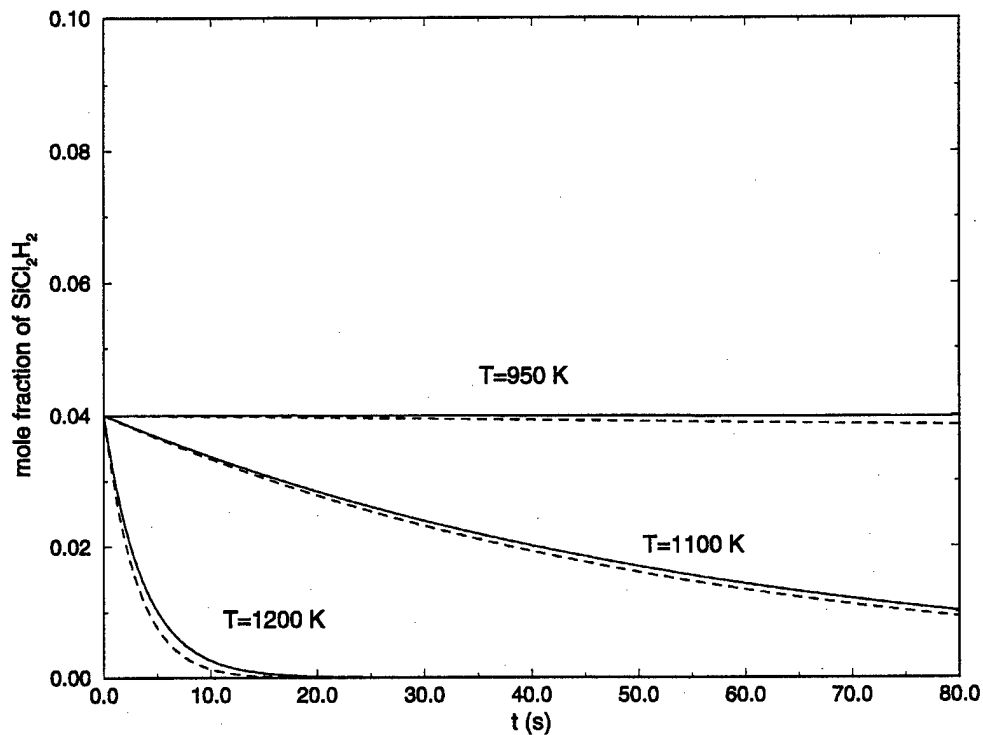
Figure 30. Concentration transients of $SiCl_2H_2$ obtained from the ODE system (solid lines) and reconstruction of the concentration transients from the projections of the data on the POD modes (dashed lines for three different temperatures T=950, 1100 and 1200 K.

5. Model-Based Control for HTS MOCVD

This section contains ideas for real-time and run-to-run controller design of a CVD reactor.

Physical Model

A 2D model has been derived that approximates the static global behavior of the commercially available STI reactor, see references [25,26]. This model constitutes seven "global" gas phase reactions, a mass conservation equation, momentum conservation equations, an energy balance equation, concentration diffusive flux equations (these are all pdes) and several algebraic relations. Most of these equations are strongly coupled. So far, the dynamical part of these equations has been neglected.

Control Objectives and the Control Problem

The ultimate objective of this type of process is to obtain a uniformly distributed metal oxide deposition of desired thickness onto a wafer. Currently, the deposition as function of the wafer radius is roughly exponential with maximum deposition at the wafer center. By placing the wafer on a susceptor with larger radius, the extreme deposition points are on the susceptor, which improves uniformity of the wafer deposition. By rotating the wafer, the minimum deposition point moves from the edge of the wafer to the center, which also improves uniformity. As a result, a concave deposition profile is obtained.

The following manipulated inputs are available to control deposition:
- flow rate and/or pressure of the carrier gas;
- temperature of the susceptor;
- concentration of the precursor gases.

The following outputs are available for monitoring deposition:
- flow rate measurement of carrier gas (*in-situ*);
- thermocouples on the wafer and/or susceptor (*in-situ*);
- deposition thickness measurements (*ex-situ*).

Expected sources of noise and disturbances are:
- measurement noise on all measurements;
- periodic disturbance from wafer rotation, e.g., because of wafer eccentricity;
- randomly occurring "drops" in flow rate;
- randomly occurring changes in precursor concentration;
- drifts in wafer and susceptor temperature;

The control problem is to obtain deposition thickness with a desired deposition uniformity using the available control inputs and measured outputs, in the face of the expected noise and disturbances.
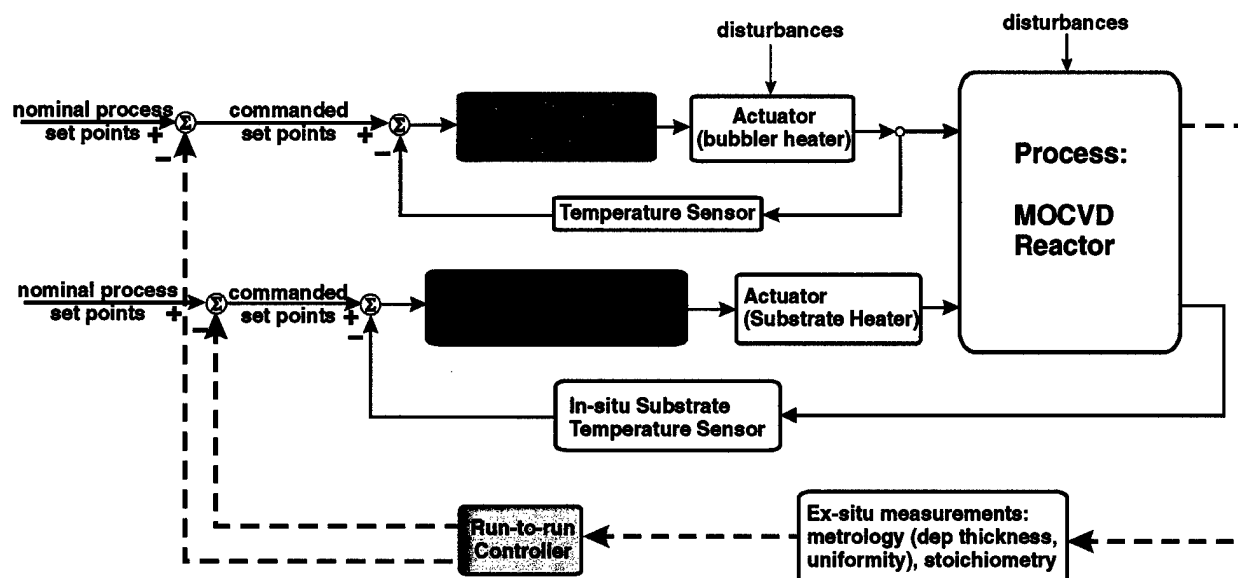
Figure 31. Schematic of Control Structure for HTS MOCVD.

Control Strategy

The deposition process as a function of control inputs can be considered as a static system. Therefore, there may be no need for a dynamic controller that tries to control deposition directly from the manipulated inputs; a desired deposition is obtained by regulating the manipulated inputs at a desired (nominal) operating point. These nominal operating points have been identified in [24]. However, all disturbances are dynamic, which implies that dynamic "slave" controllers are needed locally to obtain tight regulation at the desired operating points, see Figure 31. The control structure shows both dynamic a controller using *in-situ* sensing as well as a run-to-run controller employing *ex-situ* sensors. The bubblers are controlled by local (inner-loop) controllers, there are in-situ temperature sensors measuring substrate temperature corresponding to substrate (segmented) heaters, and metrology is employed to measure wafer properties of interest (deposition thickness and uniformity, stoichiometry).

It is expected that integral control and (notch) filtering possibly extended with some phase compensation will give tight regulation. For this design, it is preferred to have (low-complexity) dynamic models available that relate measured outputs to manipulated inputs and disturbances/noise.

To control deposition uniformity, run-to-run control has shown to be an excellent means to improve current uniformity, see reference [27], especially the example, which shows run-to-run control of a Rapid Thermal Oxidation process that has characteristics similar to CVD. The main idea is to adjust the values of the nominal operating points (called recipe variables) from wafer-to-wafer, i.e., off-line after each run, see Figure 31. For this purpose, a static model is needed that relates manipulated inputs to (*ex-situ*) measured deposition thickness. This model can be obtained with the existing CFD-ACE software by simulating the deposition process for varying values of one operating point while fixing the other operating points. For small variations it is expected that only one variation (from its nominal value) per operating point is needed. For larger variations, non-linear behavior may be taken into account by measuring deposition

44

thickness for multiple variations per operating point. The (static) map from operating points (recipe variables) to deposition thickness is called the response surface. Initially, it is sufficient to identify only the following response surfaces:

- a nominal response surface with all operating points fixed at their current nominal values;
- one response surface for each recipe variable with the operating point varied from its nominal value with very small variations (0.1 – 0.5% of nominal value).

The collection of response surfaces for each operating point is an $m \times n$ matrix with m the number of measured deposition thickness points on the wafer and n the number of recipe variables. Inversion of this matrix is the key to run-to-run control. As n is usually much less than m, the maximum obtainable uniformity level is limited. If this uniformity level is not acceptable, it is possible to improve it by increasing the number of recipe variables, e.g., by assuming that there are k (independent) temperature control inputs ("rings") in the susceptor (i.e., using heater segmentation) and obtain separate response surfaces for each temperature ring. In general, the number and choice of manipulated inputs and measured outputs can be a powerful design variable to obtain the desired goal, and it will be interesting to investigate if an "optimal" choice can be made.

Run-to-Run Control

The goal of a manufacturing system is to produce multiple copies of the same product, each having attributes within specified tolerances. Product quality attributes are typically determined after the product is manufactured, since in most cases sensors are not available which can directly monitor all of these attributes during the process. Moreover, during the run, the control variables, or recipe variables, are pre-set and held fixed during the run. Different recipes can be selected to produce different products, or similar products but with different attributes.

The run-to-run control problem is to adjust the recipe for the next run based on the results of the previous runs such that the product quality improves and/or yield increases, i.e., more good product is produced. This has proved to be very popular in process control.

In this section we describe how the recipe can be adjusted from "run-to-run" using a very simple algorithm based on the attributes of the product produced in the previous run or runs [57]. The algorithm can be analyzed under a variety of assumptions on the behavior of the actual process using standard control theory [57].

Let $t = 1,2,....$, denote the run number, $r_t \in R^m$ the vector of recipe variables used during run t, $y_t \in R^n$ the vector of product quality attributes produced at the end of run t, and e_t the normalized product quality error, whose ith element is defined as,

$$e_t(i) = (y_t(i) - y_{des}(i))/y_{tol}(i) \qquad i = 1,...,n \qquad (1)$$

where $y_{des}(i)$ is the ith desired product quality attribute, and $y_{tol}(i)$ is the associated error tolerance. The error, written in vector form, becomes,

$$e_t = R^{-1} (y_t - y_{des})$$

$$R = \text{diag} (y_{tol}(1),...,y_{tol}(n)) \qquad (2)$$

The simplest choice for run-to-run control is to correct the previous recipe by an amount proportional to the current error. Thus, for run $t = 1,2,...$, adjust the recipe according to,

$$r_t = r_{nom} + u_t$$

$$u_t = u_{t-1} - \Gamma \, e_{t-1}, \qquad u_0 = 0 \qquad\qquad (3)$$

where r_{nom} is the nominal recipe, u_t is the correction to the nominal recipe for run t, and $\Gamma \in R^{mxn}$ is the control design (gain) matrix. It is important to emphasize that (2) together with (3) constitutes the *complete* run-to-run algorithm. Observe also that (3) has the same form as a gradient descent optimization algorithm. It is possible to choose Γ and to analyze the algorithm under a variety of assumptions about how u_t effects e_t [57]. It can be shown that most of the widely used run-to-run algorithms are in the form of (3) for different choices of the control design (gain) matrix Γ.

Run-to-Run Control for MOCVD Process

In this section we will discuss application of run-to-run control to the MOCVD process. A common type of control problem in MOCVD is to control desired stoichiometries for both Ba/Y and Cu/Y by adjusting the precursor concentrations of Y, Ba and Cu, while maintaining a desired growth-rate. Hence we have three recipe variables available:

$$r = \begin{bmatrix} Y \\ Ba \\ Cu \end{bmatrix}$$

Theoretically we can have as many performance variables as we wish, but if this number is larger than the number of recipe variables, the computation of Γ will be based on the pseudo-inverse of the static relationship between performance and recipe variables, and a singular value decomposition has to be used to project the space of performance variables onto the space of recipe variables, i.e., in effect only three performance variables can be controlled. Consequently we have to select three performance variables. We choose the stoichiometries of Ba and Cu at the *center* of the wafer as the first two performance variables, and the *average* growth rate over all wafer nodes as the third:

$$y = \begin{bmatrix} S_{Ba} \\ S_{Cu} \\ R_{av} \end{bmatrix}$$

with S_{Ba} and S_{Cu} denoting the stoichiometries of Ba and Cu at the center, respectively, and R_{av} denoting the average growth-rate in Å/min.

There is no such thing as an optimal stoichiometry or optimal growth-rate, rather there are upper and/or lower bounds on the final stoichiometries and growth-rate. For this process, the following desired operating area has been identified:

$$1.5 \le S_{Ba} \le 2.0$$
$$3.0 \le S_{Cu} \le 4.0$$
$$32 \le R_{av} \le 40$$

For run-to-run control we need to have a single desired operating point, hence we pick an arbitrary point in the desired area:

$$y_{des} = \begin{bmatrix} 1.8 \\ 3.2 \\ 35 \end{bmatrix}.$$

Furthermore, we have to compute the 3x3 matrix gain Γ. For this, we identified the static relationship between perturbations in precursor concentration and the corresponding perturbation of the three performance variables. The perturbations were taken as +10% perturbations from the following nominal starting points:

$$r_{nom} \doteq \begin{bmatrix} Y_{nom} \\ Ba_{nom} \\ Cu_{nom} \end{bmatrix} = \begin{bmatrix} 0.000562038 \\ 0.002873710 \\ 0.000327275 \end{bmatrix}.$$

The corresponding nominal performance variables were computed as:

$$y_{nom} \doteq \begin{bmatrix} S_{Ba}^{nom} \\ S_{Cu}^{nom} \\ R_{av}^{nom} \end{bmatrix} = \begin{bmatrix} 5.47229 \\ 0.345701 \\ 33.2372 \end{bmatrix}$$

This resulted in the following gain matrix :

$$\Gamma = \mu \begin{bmatrix} 1.59857 & 0.675818 & -0.325193 \\ -0.370606 & 0.611552 & -0.294269 \\ 1.45349 & -28.2884 & -0.295681 \end{bmatrix}.$$

The factor μ is a number between 0 and 1, and is used to trade-off speed of convergence versus amplification of measurement noise.

We started the run-to-run iterations with $\mu = 1$. However, the solution diverged rapidly from run to run with these gains. Two reasons can account for this. Firstly, the nominal operating point is far away from the target operating point. Consequently, the run-to-run gains are large, because they are based on a large error. Secondly, the system is nonlinear while the run-to-run gains are based on a linear approximation. The combination of these two factors make it impossible to converge quickly (i.e., with $\mu = 1$) to the target operating point. Therefore we have to lower μ in order to make the iteration converge. The downside of this, however, is the fact that (a lot) more iterations are required to converge close enough to the target point. This may very well be undesirable, as more iterations mean more wafers with undesirable compositions. We therefore propose the following four-step approach:

1. Identify run-to-run gain in nominal (current) operating point using (real-time) experiments.
2. Simulate a run-to-run iteration with an approximate (linear) system model using a low value of μ and use as many iterations so as to converge with high accuracy to the desired operating point.
3. Use the optimal simulated input values as a starting point for a new experiment. Determine how much the measured performance differs from the optimal simulated performance.
4. If necessary, identify new run-to-run gains in the new operating point – which should be much closer to the target operating point – and repeat the run-to-run experiment.

We applied this four-step approach to the MOCVD process. With the identified gain Γ we started step 2, the run-to-run simulation. Figures 32 and 33 show thirty run-to-run iterations in a ternary diagram for two different values of μ, namely $\mu = 0.2$ and $\mu = 0.3$, respectively. The iteration with $\mu = 0.3$ is almost unstable, and larger values of μ indeed make the iteration diverge. Iterations with $\mu = 0.1$ (not shown) look similar to iterations with $\mu = 0.2$, except that now approximately 50 iterations are needed to reach the target point. Clearly, a run-to-run iteration with $\mu = 0.2$ converges to the target operating point with any desired accuracy. Also, the average growth-rate converged to its desired value of 35. After thirty run-to-run iterations, the performance variables converged to:

$$y_{\mu=0.2}^{30} = \begin{bmatrix} 1.95305 \\ 3.19925 \\ 35.5246 \end{bmatrix}, \quad y_{\mu=0.3}^{30} = \begin{bmatrix} 1.84445 \\ 2.93252 \\ 35.1611 \end{bmatrix}$$

We recomputed the simulation with $\mu = 0.2$, now performing 200 iterations so that the converged values reached the target value within an accuracy of 1e-5. The resulting optimal input values are given by:

$$r_{\mu=0.2}^{200} = \begin{bmatrix} 0.000931721 \\ 0.001566990 \\ 0.005022070 \end{bmatrix}.$$

With these values we performed step three of the four-step approach. We recomputed the nonlinear CFD-ACE simulation to check how much this solution would differ from the approximate solution. The resulting performance variables were given by:

$$y = \begin{bmatrix} 1.80745 \\ 3.16043 \\ 35.0786 \end{bmatrix},$$

which is very close to the desired values of 1.8, 3.2 and 35, respectively. This shows the validity of the four-step approach. In effect, only five 'expensive' experiments had to be conducted in order to converge with high accuracy to the target operating point.

Figure 34 checks how controlling the stoichiometries at the center point and controlling the average growth-rate affect the stoichiometries and the growth-rate at the other wafer nodes, respectively. Apparently, the values of the stoichiometries and the growth-rate at each wafer node lie within the desired operating range. Given the fact that the shape of the curve is very deterministic, one could similarly control one of the extreme points at the wafer edge or one of the points between the edge and the center, and check the other points afterwards. A motivation for choosing another point than the center point, might be that the other points are closer to the target point, hence convergence of the iteration will be faster. If one or more wafer nodes fall outside the desired operating range, one can change the target operating point and shift it to a position inside the desired area where all wafer nodes meet the specification, or one can control another wafer node. If desired, one can control different wafer nodes for Ba and Cu stoichiometries.
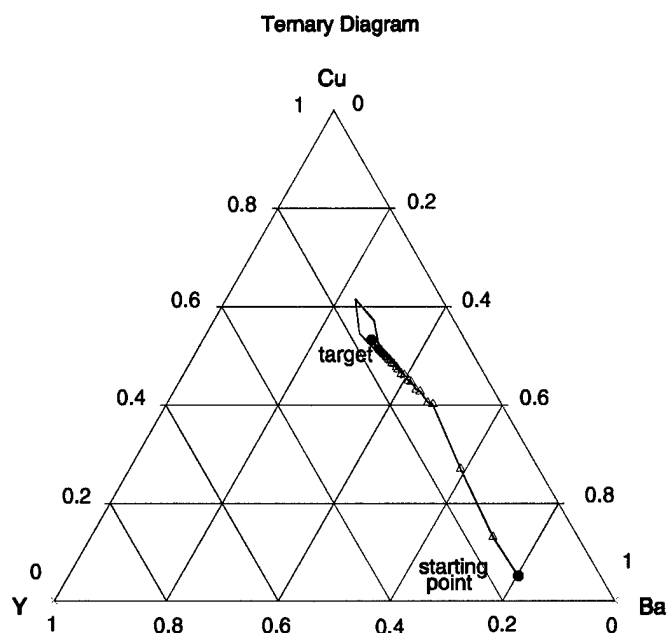
Figure 32. Ternary diagram showing 30 run-to-run iterations from the nominal starting point to the target operating point with $\mu = 0.2$. The starting point and target point are shown as a thick green and red bullet, respectively, while the iterations are shown as small triangles. Also shown in red is the desired operating area.
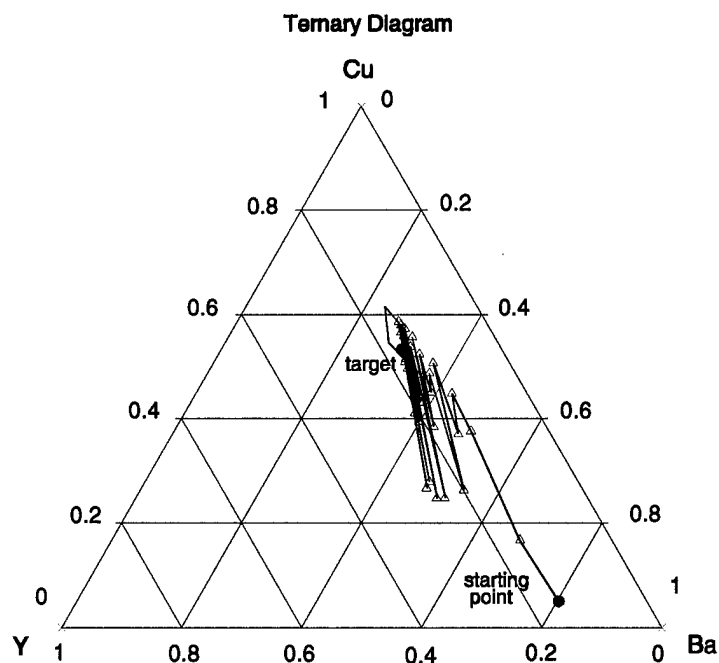
Figure 33. Ternary diagram showing 30 run-to-run iterations from the nominal starting point to the target operating point with $\mu = 0.3$. The starting point and target point are shown as a thick green and red bullet, respectively, while the iterations are shown as small triangles. Also shown in red is the desired operating area.

49
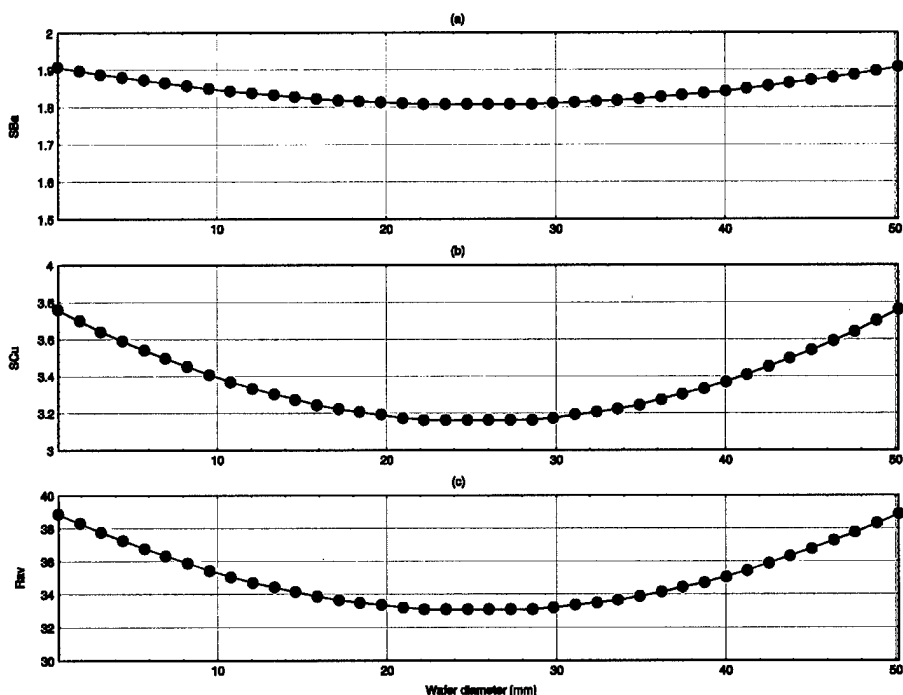
Figure 34. Final performance for all wafer nodes along the wafer diameter. (a) Ba stoichiometry; (b) Cu stoichiometry; (c) growth-rate.

The implication of this result is very significant. It suggests that it is possible to speed up the run-to-run control by performing the run-to-run iterations in the simulation (rather than experiment) and only apply control to the actual chamber once the stoichiometry is within the desired region. The run-to-run control iterations via the virtual chamber avoid the cost associated with the use of actual wafers and increase throughput significantly as well as improving reproducibility. Even if the run-to-run control cannot provide the desired stoichiometry on the first try, it will provide the ability to get much closer to the desired stoichiometry region than would otherwise be possible.

6. Conclusions

We have developed a systematic methodology to look at the structure and reactivity of the metal β-diketonates precursors, used in the chemical vapor deposition of high temperature superconductors, using first principle quantum chemistry methods. The large size of the precursor molecules has so far limited studies of this nature. Very little information is available on the chemistry of these compounds. Semi-empirical methods were found inadequate in describing the structures and traditional ab-initio methods were deemed to be very expensive, given the size of the molecules. We have tested and validated different density functionals for describing these molecules. Based on our validations, an effective core potential was chosen to describe the metal (Cu and Y). We have investigated the decomposition mechanism for $Cu(acac)_2$ and $Cu(dpm)_2$, two of the most common precursors for copper in HTS films. A kinetic mechanism for decomposition was formulated and the initial break-up of the Cu-O bond was determined to be the rate-limiting step. A similar investigation was also carried out for $Y(acac)_2$, which serves as a model for $Y(dpm)_3$. A preliminary mechanism has been put together based on the work done so far.

Results have been obtained for reactor-scale physical modeling of MOCVD of YBCO. The model includes chemical kinetics and species transport to the wafer surface. The YBCO deposition rates obtained from these simulations are comparable to those published in the literature. Sensitivity calculations using this model were used for run-to-run controller design.

A general control structure was developed for MOCVD reactor control. An innovative run-to-run control method was developed which enables efficient stoichiometry control. A standard run is performed and performance measures are determined using ex-situ metrology. The run-to-run control iterations are then run on the virtual reactor model to suggest control perturbations for the next actual run to reach the desired stoichiometry region.

7. Future Work

Further work needs to be done to get a more detailed picture of the decomposition pathways. In particular, the effect of the oxidant gas such as O_2 and N_2O, if any, needs to be explored further. In this study, we have concentrated our attention on copper precursors due to the computational efforts involved in study of larger molecules such as yttrium and barium. A similar detailed treatment needs to be carried out for yttrium precursors and eventually extended to barium precursors. Yttrium precursors are known to coordinate a water molecule to give $Y(dpm)_3.H_2O$ molecule [1]. The effect of this coordination on the decomposition pathways needs to be explored further.

The detailed models need to be reduced for reactor modeling, simulation, and control design. We will continue investigating the application of POD and other model-order reduction methods to the full chemical-transport model.

The refined kinetic mechanism obtained from the yttrium and barium calculations need to be incorporated into the reactor scale model. The predictions of the reactor scale model need to be validated against the experimental results such as those planned as part of the Caltech VIP effort.

The procedures used in this work could be expanded to ferroelectrics, such as $BaSrTiO_3$, since similar MOCVD precursors are used [58]. The chemistry of MOCVD of ferroelectrics is not well understood, yet there is a considerable interest in using these materials in ULSI IC production. A detailed study of the basic reaction pathways and rates, similar to the one performed for HTS, would provide the necessary data for simulation of MOCVD of ferroelectrics.

8. Appendix I. Data for the Quantum Chemistry Validation Study

Cu

Excitation energies Eexec and ionization potentials IP for Cu 2S with different basis sets and methods [eV]

		E_{exec}	I.P.
ECP1	CAS	-2.88	
	B3LYP	8.00	7.94
	CCSD(T) (3d/4s) [a]	1.69	6.91
ECP2	CAS	-3.00	
	B3LYP	6.77	8.68
	CCSD(T) (3d/4) [a]	1.32	6.88
	CCSD(T)	1.82	6.85
	CCSD(T) [b]	1.65	7.13
ECP-S[28]	CAS	-3.12	
	B3LYP	7.01	8.66
	CCSD(T) (3d/4s) [a]	1.47	7.07
	CCSD(T)	1.76	7.04
Experimental [46]		1.49	7.73

[a] includes only correlation between the 3d and 4s/p shell
[b] additional d and f function

Ionization potentials for Cu 2S with different basis sets and methods [eV]

	BLYP	B3LYP	LSDA
6-311G	4.15	6.86	8.06
6-311+G	8.18	8.02	8.82
6-311G**	7.78	7.48	8.06
6-311+G**	8.18	8.02	8.82
ECP1	7.67	7.67	8.27
ECP2	9.33	7.82	8.53

CuH

Method	Basis Set	r_e	ω	D_e [eV]
CI	all-electron	1.59	1584	2.36 [47]
CI(cv)		1.50	1740	2.49
CI(cc)		1.51	1815	2.42
B3lYP	ECP1	1.51	1868	3.29
	ECP2	1.50	1837	2.73
	6311+G**	1.48	1879	2.69
Exp.		1.46	1941	2.85

CuMe, CuEt

Dissociation energies [De] for CuMe and CuEt [kcal/mol]
CuMe
experimental: about 60 kcal/mol
other theoretical work: Bauschlicher [48] 45.8
                                Ziegler   [49] 56.8
                                Boehme   [31] 58.0

Method	Basis Set	CuMe	CuEt
B3LYP	6-311G		78.82
	6-311+G		45.25
	6-311G**		65.78
	6-311+G**	52.37	45.98
	Ahlrichs TZV		
	ECP1	59.09	53.80
	ECP2	53.66	48.01
LSDA	6-311G		
	6-311+G		
	6-311G**		
	6-311+G**	78.17	70.89
	ECP1	90.59	84.64
	ECP2	81.04	74.82
BLYP	6-311G		
	6-311+G		
	6-311G**		
	6-311+G**	56.96	50.85
	ECP1	69.09	63.78
	ECP2	25.71	20.49

BSSE for CuMe using B3LYP [kcal/mol]

Basis Set	BSSE	corrected D_e	uncorrected D_e
6-311+G**	-5.56	57.93	52.37
ECP1	7.95	51.14	59.09
ECP2	-2.89	56.55	53.66

Comparison of calculated and experimental CuMe frequencies

	calculated frequencies			Experimental vibrations	theo/exp		
B3LYP	6-311+G**	ECP1	ECP2		6-311+G**	ECP1	ECP2
Cu-Me str	522	510	533	350	1.49	1.46	1.52
Cu-Me tilt	674	735	692	424	1.59	1.73	1.63
CH sy-b	1122.7	1293.8	1152				
CH as-b	1445.2	1600.7	1469	1336	1.08	1.20	1.10
CH as-str	3126.3	3447.4	3158	2929	1.07	1.18	1.08
CH sy-str	3030.6	3269.6	3036	2880	1.05	1.14	1.05
BLYP	6311pss	MB	DZ				
Cu-Me str	516	507	530		1.47	1.45	1.51
Cu-Me tilt	671	722	683		1.58	1.70	1.61

	6311pss	MB	DZ			
CH sy-b	1092	1248	1120			
CH as-b	1406	1547	1426	1.05	1.16	1.07
CH as-str	3054	3334	3082	1.04	1.14	1.05
CH sy-str	2959	3159	2961	1.03	1.10	1.03
LSDA	6311pss	MB	DZ			
Cu-Me str	590	586	603	1.69	1.67	1.72
Cu-Me tilt	648	737	685	1.53	1.74	1.62
CH sy-b	1060	1260	1115			
CH as-b	1358	1535	1397	1.02	1.15	1.05
CH as-str	3083	3407	3116	1.05	1.16	1.06
CH sy-str	2971	3228	2981	1.03	1.12	1.04

Calculated harmonic fundamentals for CuEt

B3LYP	6311G	6311+G	6311G**	6311+G**	ECP1	ECP2
	230	226	228	222	222	222
Cu-C str	268	230	267	230	232	223
	552	492	547	487	475	498
	688	636	655	618	662	634
	938	935	914	914	990	917
	982	968	954	947	1029	966
Cu-C-C b	1023	1010	1019	1010	1118	1022
	1236	1180	1195	1152	1270	1168
	1272	1261	1248	1240	1340	1246
	1452	1439	1412	1403	1558	1427
	1492	1491	1456	1458	1607	1478
	1533	1533	1493	1493	1666	1517
CH b asym	1539	1538	1494	1498	1671	1525
CH3 str einzel	2971	2964	2983	2979	3277	3001
CH2 str symm	3002	3003	3021	3027	3290	3044
CH2 str asym	3046	3043	3056	3054	3397	3088
CH3 str symm	3048	3050	3063	3069	3432	3103
CH3 str asy	3084	3083	3091	3092	3473	3133

Calculated harmonic fundamentals for CuEt (relative to 6-311G)

B3LYP	6311+G	6311G**	6311+G**	ECP I	ECP II
	0.98	0.99	0.97	0.96	0.97
Cu-C str	0.86	1.00	0.86	0.86	0.83
	0.89	0.99	0.88	0.86	0.90
	0.93	0.95	0.90	0.96	0.92
	1.00	0.97	0.97	1.06	0.98
	0.99	0.97	0.96	1.05	0.98
Cu-C-C b	0.99	1.00	0.99	1.09	1.00
	0.95	0.97	0.93	1.03	0.95
	0.99	0.98	0.97	1.05	0.98
	0.99	0.97	0.97	1.07	0.98

	1.00	0.98	0.98	1.08	0.99
	1.00	0.97	0.97	1.09	0.99
CH b asym	1.00	0.97	0.97	1.09	0.99
CH3 str einzel	1.00	1.00	1.00	1.10	1.01
CH2 str symm	1.00	1.01	1.01	1.10	1.01
CH2 str asym	1.00	1.00	1.00	1.12	1.01
CH3 str symm	1.00	1.01	1.01	1.13	1.02
CH3 str asy	1.00	1.00	1.00	1.13	1.02

CuO

Dissociation energies D_e [kcal/mol]

Method	Basis Set	D_e CuO
LSDA	6-311G	113.4
	6-311+G	118.1
	6-311G**	92.5
	6-311+G**	97.1
	ECP I	84.0
	ECP II	91.1
BLYP	6-311G	170.4
	6-311+G	173.3
	6-311G**	70.0
	6-311+G**	72.6
	ECP I	66.7
	ECP II	70.3
B3LYP	6-311G	75.3
	6-311+G	78.8
	6-311G**	59.1
	6-311+G**	61.7
	ECP I	45.0
	ECP II	58.0
Experimental[50]		62.7 ∀ 3.0

9. Appendix II: Publications

<u>Journal Papers:</u>

1. "A Density Functional Theory Study of (Hfac)Cu-L Compounds of interest for the Chemical Vapor Deposition of Copper," Carlo Cavallotti, Vijay Gupta, Cornelia Sieber and Klavs F. Jensen, to be submitted to *Journal of Physical Chemistry*.
2. "Computational Chemistry Investigations of Precursor Decomposition Pathways in MOCVD of High Temperature Superconductors," Vijay Gupta and Klavs F. Jensen, to be submitted to *Journal of Crystal Growth*.

<u>Conference Presentation:</u>

1. S. Ghosal, J. L. Ebert, D. de Roover, and A. Emami-Naeini, "Model-based Control of MOCVD Rate, Uniformity and Stoichiometry," Presented at the Third Symposium of Process Control, Diagnostics, and Modeling in Semiconductor Manufacturing, *195th Meeting of the Electrochemical Society*, Seattle, May 2--6, 1999.

10. References:

[1] P. J. Hay and W. R. Wadt, *Journal of Chemical Physics*, vol. 82, pp. 270, 1985.

[2] P. J. Hay and W. R. Wadt, *Journal of Chemical Physics*, vol. 82, pp. 299, 1985.

[3] W. R. Wadt and P. J. Hay, *Journal of Chemical Physics*, vol. 82, pp. 284, 1985.

[4] M. Svensson, S. Humbel, R. D. J. Froese, T. Matsubara, S. Sieber, and K. Morokuma, *Journal of Physical Chemistry*, vol. 100, pp. 19357, 1996.

[5] M. Leskela, H. Molsa, and L. Niinisto, *Superconductor Science and Technology*, vol. 6, pp. 627-656, 1993.

[6] B. J. Hinds, R. J. McNeely, D. B. Studebaker, T. J. Marks, T. P. Hogan, J. L. Schindler, C. R. Kannewurf, X. F. Zhang, and D. J. Miller, *Journal of Materials Research*, vol. 12, pp. 1214-1236, 1997.

[7] I. M. Watson, *Chemical Vapor Deposition*, vol. 3, pp. 9-26, 1997.

[8] K. H. Dahmen and T. Gerfin, *Progress in Crystal Growth and Characterization*, vol. 27, pp. 117-161, 1993.

[9] T. Tsuruoko, R. Kawasaki, and H. Abe, *Japanese Journal of Applied Physics*, vol. 28, pp. L1800, 1989.

[10] H. Ohnishi, K. I. Hanaoka, Y. Goto, H. Harima, and K. Tachibana, *Physica C*, vol. 190, pp. 134, 1991.

[11] M. Leskela, J. K. Truman, C. H. Mueller, and P. H. Holloway, *Journal of Vacuum Science and Tecnology A*, vol. 7, pp. 3147-3171, 1989.

[12] F. Westley, "Table of Recommended Rate Constants for Chemical Reactions Occurring in Combustion," National Bureau of Standards NSRDS-NBS 67, 1980.

[13] M. J. Frisch, G. W. Trucks, H. B. Schlegel, G. E. Scuseria, M. A. Robb, J. R. Cheeseman, V. G. Zakrzewski, J. J. A. Montgomery, R. E. Stratmann, J. C. Burant, S. Dapprich, J. M. Millam, A. D. Daniels, K. N. Kudin, M. C. Strain, O. Farkas, J. Tomasi, V. Barone, M. Cossi, R. Cammi, B. Mennucci, C. Pomelli, C. Adamo, S. Clifford, J. Ochterski, G. A. Petersson, P. Y. Ayala, Q. Cui, K. Morokuma, D. K. Malick, A. D. Rabuck, K. Raghavachari, J. B. Foresman, J. Cioslowski, J. V. Ortiz, B. B. Stefanov, G. Liu, A. Liashenko, P. Piskorz, I. Komaromi, R. Gomperts, R. L. Martin, D. J. Fox, M. T. Keith, A. Al-Laham, C. Y. Peng, A. Nanayakkara, C. Gonzalez, M. Challacombe, P. M. W. Gill, W. C. B. Johnson, M. W. Wong, J. L. Andres, C. Gonzalez, M. Head-Gordon, E. S. Replogle, and J. A. Pople, "Gaussian 98, Revision A.5.," . Pittsburgh, PA: Gaussian, Inc., 1998.

[14] MOLPRO, is a package of ab initio programs written by H. -J. Werner, Knowles, R. D. Amos, A. Berning, D. L. Cooper, M. J. O. Deegan, A. J. Dobyn, F. Eckert, S. T. Elbert, C. Hampel, R. Lindh, A. W. Lloyd, W. Meyer, A. Nicklas, K. Peterson, R. Pitzer, A. J. Stone, P. R. Taylor, M. E. Mura, P. Pulay, M. Schuetz, H. Stoll, and T. Thorsteinsson .

[15] A. D. Becke, *Physical Review. A*, vol. 38, pp. 3098, 1988.

[16] C. Lee, W. Yang, and R. G. Parr, *Physical Review B*, vol. 37, pp. 785, 1988.

[17] I. Komaromi, S. Dapprich, K. S. Byun, K. Morokuma, and M. J. Frisch, (in prep), 1998.

[18] S. Dapprich, I. Komaromi, K. S. Byun, K. Morokuma, and M. J. Frisch, *Theochem-Journal of Molecular Structure*, vol. 462, pp 1-21, 1999.

[19] J. Yu, E. Adei, and W. J. Hehre (unpublished).

[20] Spartan 5.0, Wavefunction, Inc. 18401 Von Karman Ave., Ste. 370 Irvine, CA 92612 U.S.A.

[21] S. Shibata and K. Sone, *Bulletin of the Chemical Society of Japan*, vol. 29, pp. 852-856, 1956.

[22] S. Shibata, S. Takafumi, and M. Ohta, *Journal of Molecular Structure*, vol. 96, pp. 345-352, 1983.

[23]   A. D. Becke, *Journal of Chemical Physics*, vol. 98, pp. 5648, 1993.

[24]   J. C. Slater, in *Quantum Theory of Molecular Fluids and Solids*, vol. 4. New York: McGraw-Hill, 1974.

[25]   W. Kohn and L. J. Sham, *Physical Review*, vol. 140, pp. A1133, 1965.

[26]   P. Hohenberg and W. Kohn, *Physical Review*, vol. 136, pp. B864-B871, 1964.

[27]   S. H. Vosko, L. Wilk, and M. Nusair, *Canadian Journal of Physics*, vol. 58, pp. 1200, 1980.

[28]   M. Dolg, U. Wedig, H. Stoll, and H. Preuss, *Journal of Chemical Physics*, vol. 86, pp. 866-872, 1987.

[29]   Q. Cui, D. G. Musaev, M. Svensson, and K. Morokuma, *Journal of Physical Chemistry*, vol. 100, pp. 10936, 1996.

[30]   T. a. o. Ziegler, *Journal of the American Chemical Society*, vol. 109, pp. 1351, 1987.

[31]   M. Boehme and G. Frenking, *Chemical Physics Letters*, vol. 224, pp. 195, 1994.

[32]   S. Shibata, K. Iijima, and T. Inuzukz, *Journal of Molecular Structure*, vol. 144, pp. 181-184, 1986.

[33]   N. V. Belova, N. I. Giricheva, G. V. Girichev, S. A. Shlykov, E. V. Kharlanova, N. P. Kuzmina, and K. A. R., *Journal of Structural Chemistry*, vol. 38, pp. 395-402, 1997.

[34]   K. K. Irikura, *International Journal of Mass Spectrometry*, vol. 185-187, pp. 577-587, 1999.

[35]   M. A. V. R. Silva, M. Luisa, and C. C. H. Ferrao, *Pure and Applied Chemistry*, vol. 60, pp. 1225-1234, 1988.

[36]   A. Y. Kovalgin, F. Chabert-Rocabois, M. L. Hitchman, S. H. Shamlian, and S. E. Alexandrov, *Journal de Physique IV*, vol. 5, pp. 357-364, 1995.

[37]   G. G. Condorelli, M. L. Hitchman, A. Y. Kovalgin, and S. H. Shamlian, presentation at Chemical Vapor Deposition and EUROCVD-11, 1997.

[38]   T. K. Choudhury and M. C. Lin, *International Journal of Chemical Kinetics*, vol. 20, pp. 491-504, 1990.

[39]   A. F. Bykov, P. P. Semyannikov, and I. K. Igumenov, *Journal of Thermal Analysis*, vol. 38, pp. 1463-1475, 1992.

[40]   K. Hanaoka, H. Ohnishi, and K. Tachibana, *Japanese Journal of Applied Physics, Part I*, vol. 32, pp. 4774-4778, 1993.

[41]   A. Jain, T. T. Kodas, T. S. Corbitt, and M. J. Hampden-Smith, *Chemistry of Materials*, vol. 8, pp. 1119-1127, 1996.

[42]   A. E. Turgambaeva, A. F. Bykov, and I. K. Iguemnov, *Journal de Physique IV*, vol. C5, pp. C5-22 - C5-228, 1995.

[43]   E. A. Mazurenko, V. Y. Zub, S. L. Voroginskii, and S. V. Volkov, *Ukr. Khim. Zh.*, vol. 54, pp. 1235, 1988.

[44]   J. Pinkas, J. C. Huffman, D. V. Baxter, M. H. Chisholm, and K. G. Caulton, *Chemistry of Materials*, vol. 7, pp. 1589-1596, 1995.

[45]   G. V. Girichev, N. I. Giricheva, N. V. Belova, K. A. R., N. P. Kuz'mina, and O. Y. Gorbenko, *Russian Journal of Inorganic Chemistry*, vol. 38, pp. 320-323, 1993.

[46]   *CRC Handbook of Chemistry and Physics*. Boca Raton (FL): CRC Press, 1996.

[47]   L. G. M. Petterson and H. Akeby, *Journal of Chemical Physics*, vol. 94, pp. 2968, 1991.

[48]   C. W. Bauschlicher, S. R. Langhoff, H. Partridge, and L. A. Barnes, *Journal of Chemical Physics*, vol. 91, pp. 2399-2411, 1989.

[49]   T. Ziegler, V. Tschinke, and A. Becke, *Journal of the American Chemical Society*, vol. 109, pp. 1351-1358, 1987.

[50]   M. W. J. Chase, *NIST JANAF Thermochemical Tables*, vol. 14. Washington, D.C., 1998.

[51]   H. A. Luten, W. S. Rees Jr., and V. L. Goedken, *Chemical Vapor Deposition*, vol. 2, pp. 149-161, 1996

[52]   M. Habuka, Katayama, M. Shimda, K. Okuyama, "Numerical Evaluation of

Silicon Thin Growth from $SiHCl_3$-H_2 Gas Mixture in a Horizontal Chemical Vapor Deposition Reactor," *Jpn. J. Appl. Phys.*, 1994. **33**: p.1977-1985.

[53]   L. Raja, Colorado School of Mines, private communication, 1998.

[54]   A. Emami-Naeini et al., *Modeling and Control for Rapid Thermally Driven Deposition Processes*. September 1998 Technical Progress Report. SC Report No.: CVD-002, September 21, 1998

[55]   A. Emami-Naeini et al., *Modeling and Control for Rapid Thermally Driven Deposition Processes*. December 1998 Technical Progress Report. SC Report No.: CVD-003, December 21, 1998.

[56]   A. Emami-Naeini et al., *Modeling and Control for Rapid Thermally Driven Deposition Processes*. December 1998 Technical Progress Report. SC Report No.: CVD-004, March 21, 1998.

[57]   R. Kosut, D. de Roover, A. Emami-Naeini, J. L. Ebert, "Run-to-Run Control of Static Systems," in *Proc. 37th IEEE Conf. Decision Control*, December 1998.

[58]   M. Kiyotoshi, et al., "In-situ Muti-step (IMS) CVD Process of (Ba, Sr)TiO3 using Hot Wall Batch Type Reactor for DRAM Capacitor Dielectrics," *Symp. VLSI Tech. Dig.*, pp. 101-102, 1999.

[59]   W. R. Rees, (Ed), *CVD of Non-metals*, 1993, VCH, Weinhem.

[60]   K. F. Jensen, *Transport Phenomena in Vapor Phase Epitaxy Reactors*. Handbook of Crystal Growth 3, Part B, 1994. p. 593-598. Ed: D. T. J. Hurle, Elsevier, Amsterdam.

[61]   M. Leskela, H. Molsa, and L. Niinisto, *Chemical vapour deposition of high-T_C superconducting thin films*. Superconductor Science and Tecnology, 1993. **6**: p. 627-656.

[62]   K. H. Dahmen, and T. Gerfin, *MOCVD of high-T_C superconducting materials*. Progress in Crystal Growth and Characterization, 1993. **27**: p. 117-161.

[63]   CFD-ACE Theory Manual, CFD Research Corporation, Huntsville, AL, 1998.

[64]   Van Doormal, J. P., and G. D. Raithby, *Enhancement of the SIMPLE Method for Predicting Incompressible Fluid Flows*, Numerical Heat Transfer, 1984, **7**: p. 147-163.

[65]   R. B. Bird, W. E. Stewart, and E. N. Lightfoot, *Transport Phenomena*, 1960, Wiley, New York.

[66]   F. Schmaderer, and G. Wahl , "CVD of Superconductive $YB_2Cu_3O_{7-x}$," *Journal de Physique* C5, C5-119-129, 1989.

[67]   K. Kanehori, N. Sughi, T. Fukazawa, K. Miyauchi, "Low Temperature Growth of Superconducting $YBa_2Cu_3O_{7-x}$ Thin Films by Organometallic Chemical Vapour Deposition," *Thin Solid Films*, 182 , pp. 265-269, 1989.

[68]   H. Yamane, M. Hasei, H. Kurosawa, T. Hirai, "Low Temperature Deposition of Y-Ba-Cu-O Superconducting Films by Thermal Chemical Vapor Deposition," *Japanese Journal of Applied Physics*, Vol. 30, No. 6A, June 1991.